AGU PUBLICATIONS

JGR

Journal of Geophysical Research: Solid Earth

RESEARCH ARTICLE
10.1002/2017JB014304

Key Points:
- Surface-tunnel-surface seismic experiment was conducted at the Äspö Hard Rock Laboratory in Sweden
- Tomography results image the rock mass between the tunnel and the surface, as well as fracture systems
- Strong *P-S* and *S-P* mode conversions are observed from the fracture zones and their V_p, V_s, Q_p, Q_s, V_p/V_s, and Poisson's ratio estimated

Correspondence to:
B. Brodic,
bojan.brodic@geo.uu.se

Citation:
Brodic, B., A. Malehmir, and C. Juhlin (2017), Delineating fracture zones using surface-tunnel-surface seismic data, *P-S*, and *S-P* mode conversions, *J. Geophys. Res. Solid Earth*, *122*, doi:10.1002/2017JB014304.

Received 9 APR 2017
Accepted 23 JUN 2017
Accepted article online 27 JUN 2017

Delineating fracture zones using surface-tunnel-surface seismic data, *P-S*, and *S-P* mode conversions

B. Brodic[1], **A. Malehmir**[1], **and C. Juhlin**[1]

[1]Department of Earth Sciences, Uppsala University, Uppsala, Sweden

Abstract A surface-tunnel-surface seismic experiment was conducted at the Äspö Hard Rock Laboratory to study the seismic response of major fracture systems intersecting the tunnel. A newly developed three-component microelectromechanical sensor-based seismic landstreamer was deployed inside the noisy tunnel along with conventional seismic receivers. In addition to these, wireless recorders were placed on the surface. This combination enabled simultaneous recording of the seismic wavefield both inside the tunnel and on the surface. The landstreamer was positioned between two geophone-based line segments, along the interval where known fracture systems intersect the tunnel. First arrival tomography produced a velocity model of the rock mass between the tunnel and the surface with anomalous low-velocity zones correlating well with locations of known fracture systems. Prominent wave mode converted direct and reflected signals, *P-S* and *S-P* waves, were observed in numerous source gathers recorded inside the tunnel. Forward travel time and 2-D finite difference elastic modeling, based on the known geometry of the fracture systems, show that the converted waves are generated at these systems. Additionally, the landstreamer data were used to estimate V_p/V_s, Poisson's ratio, and seismic attenuation factors (Q_p and Q_s) over fracture sets that have different hydraulic conductivities. The low-conductivity fracture sets have greater reductions in *P* wave velocities and Poisson's ratio and are more attenuating than the highly hydraulically conductive fracture set. Our investigations contribute to fracture zone characterization on a scale corresponding to seismic exploration wavelengths.

1. Introduction

The seismic response of fractures and cracks has interested the hard rock seismic exploration community since the early works of *O'Connell and Budiansky* [1974], *Hudson* [1981], and *Mair and Green* [1981]. Fractured media have strong effects on seismic wave propagation, such as causing shear wave birefringence, scattering, and attenuation or changes in the elastic parameters [*Crampin*, 1981; *Hudson*, 1981; *Eaton et al*., 2003]. In addition to these, oriented fractures are considered to be a common cause for seismic anisotropy [*Thomsen*, 1986; *Yardley and Crampin*, 1991; *Thomsen*, 2002]. Apart from the influence on seismic properties, fractures in crystalline rock environments act as conduits for gas and fluid migration, hence affecting the local stress field, the hydrogeological regime, underground infrastructures, and drilling and mining activities, among others. When the fractures are saturated with a compressible fluid or gas, the media may be highly attenuating [*Anderson et al*., 1974; *O'Connell and Budiansky*, 1974; *Johnston et al*., 1979; *Mavko and Nur*, 1979; *Mukerji and Mavko*, 1994]. Compared to laboratory studies, sonic logging, or studies conducted using vertical seismic profiling (VSP), there are few reports on seismic field experiments that investigate the relation between the permeability of fractures and their seismic response [*Green and Mair*, 1983; *Paulsson et al*., 1985; *Juhlin*, 1995b; *Lundberg et al*., 2012; *Liu and Martinez*, 2013]. To address some of the above-mentioned issues, we conducted a novel surface-tunnel-surface seismic survey at the Äspö Hard Rock Laboratory (HRL) in southern Sweden during April 2015. Well-documented fracture systems, extending from the surface and intersecting the tunnel at different depths [*Kornfält and Wikman*, 1988; *Kornfält et al*., 1997; *Rhén et al*., 1997; *Berglund et al*., 2003], provided a unique opportunity to evaluate their seismic response using a digital three-component (3C) seismic landstreamer [*Brodic et al*., 2015; *Malehmir et al*., 2015a, 2015b] in the tunnel. Both sources and receivers were located on the surface and inside the tunnel and the seismic wavefield simultaneously recorded on all receivers. Compared to other published experiments addressing the seismic response of fractures [*Maurer and Green*, 1997; *Angioni et al*., 2003; *Gritto et al*., 2003; *Daley et al*., 2004; *Gritto et al*., 2004; *Dietrich and Tronicke*, 2009; *Martínez and Mendoza*, 2011], the use of sources both inside the rock mass and on the surface makes this study rather unique. Our primary objectives were

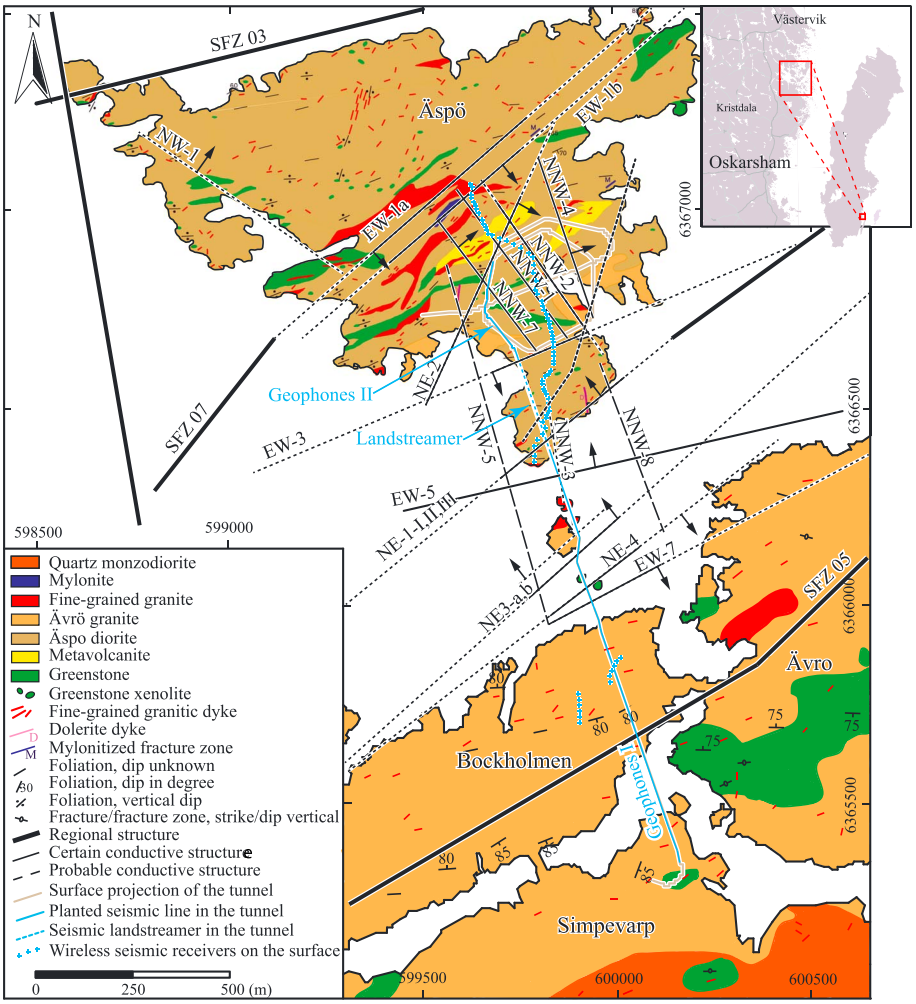

Figure 1. Geographical location, geological and structural map of the Äspö HRL site, with surface projection of the tunnel track and the location of the seismic stations inside the tunnel and wireless receivers on the surface shown. The arrows show the dip direction of the structures while the structure orientation corresponds to true azimuth. The NE-1 and EW-3 fracture systems were the primary targets of the seismic study. Also shown are mapped occurrences of foliations with their dip angles and occurrences of fine-grained granitic dikes. The white regions represent the sea surrounding the island.

1. high-resolution fracture zone delineation in underground facilities using the seismic method and checking the performance of the seismic landstreamer inside the rock mass,
2. estimating elastic properties and seismic attenuation of the fracture zones with different hydraulic properties and host rock at the site,
3. studying and modeling the seismic response and wave mode conversions observed in the vicinity of the fracture systems,
4. characterization of the rock mass between the tunnel and surface by first arrival travel time tomography given the unique acquisition geometry, and
5. verifying the capability of the digital-based seismic sensors in a highly electromagnetically noisy environment in comparison with traditional geophone-type sensors.

2. Äspö Hard Rock Laboratory

The Äspö HRL is an underground research facility located in southeastern Sweden (Figure 1), operated by the Swedish Nuclear Fuel and Waste Management Company (SKB). It was established at the end of the 1980s, with the goal of studying the properties and behavior of rock masses, testing methods for storage of spent nuclear fuel, characterization of prospective repository sites, and development and testing of new

characterization methods in the crystalline environment [*Berglund et al*., 2003]. The laboratory consists of several facilities on the surface and about 3.6 km of tunnels at different levels. From the surface (approximately 15 m above sea level), the main access tunnel goes for approximately 1.6 km downward reaching an elevation of −230 m below sea level. After this, it spirally continues downward until it reaches the final −450 m level. An elevator shaft connects the main facility building on the surface and different tunnel depths within this spiral part.

Geologically, Äspö is located predominantly within the metamorphosed granitoid-volcanic rocks of Småland-Värmland [*Kornfält et al*., 1997; *Stanfors et al*., 1999; *Stephens*, 2009; *Lundberg and Juhlin*, 2011; *Lundberg*, 2014]. The oldest rocks in the area formed during the Svecokarelian orogeny (1.85–1.65 Ga) with periods of alkali-calcic magmatism. They are represented by granitoidic to dioritoidic and gabbroidic rocks and fine-grained granitic or aplitic dikes emplaced at around 1.45 Ga. The Sveconorwegian orogeny (1.1–0.9 Ga) was coeval with the emplacement of dolerite dikes that are up to 10 m in thickness. The youngest rocks in the area are meta-sandstones deposited during the Late Precambrian, Early Cambrian period [*Kornfält and Wikman*, 1988; *Gustafson et al*., 1989; *Kornfält et al*., 1997; *Berglund et al*., 2003]. Metamorphic overprinting resulted in structural, mineralogical, and chemical changes, all contributing to the complex geology of the area. Recently, glacial processes have modified the area, giving the present-day surface consisting of exposed bedrock and occurrences of moraines and glacial sediments of up to 5 m in thickness [*Kornfält and Wikman*, 1988].

On a local scale, two rock types are dominant, along with the occurrences of fine-grained, intermediate rocks and dikes of fine-grained granite and pegmatite [*Kornfält et al*., 1997; *Rhén et al*., 1997; *Berglund et al*., 2003]. These are Ävrö granites (densities 2640–2700 kg/m^3) and Äspö diorites (densities 2700–2800 kg/m^3). Figure 1 shows the geographical location of the site, major geological units, and structural features of the Äspö HRL. The geological information is based on site-scale geological mapping, open trenches, drill cores, information from the tunnel, and geophysical information [*Kornfält and Wikman*, 1988; *Kornfält et al*., 1997; *Rhén et al*., 1997; *Berglund et al*., 2003; *Rønning et al*., 2003; *Wahlgren et al*., 2006]. Tectonic features shown represent their surface intersections inferred in the same way. Reports on hydraulic conductivity are based on direct observations in the tunnel and drilling [*Rhén et al*., 1997; *Berglund et al*., 2003].

The approximately 1.85 Ga complex structural history of the region has resulted in the formation of several deformation zones at the Äspö HRL site. *Stanfors et al.* [1999] defines seven different tectonic episodes during this period. The deformation zones commonly consist of several parallel fracture sets with different degrees of alteration and hydraulic properties, where dip angles and widths change with depth [*Rhén et al*., 1997; *Berglund et al*., 2003]. Some of the fracture systems are estimated to be more than 10 km long and extend to at least 1.5 km depth [*Rhén et al*., 1997]. Among the structures shown in Figure 1, we focus here on the NE-1 and EW-3 fracture systems crossed by the seismic recorders in the tunnel. According to *Ask* [2006] and *Andersson* [2007], where the two fracture systems of interest are encountered in the tunnel, the major principal stress (σ_1) has a magnitude of 25–35 MPa, trending 310°, and a plunge of 0–30°. Magnitude of the intermediate principal stress (σ_2) ranges from 10 to 17 MPa, with the direction of 90° and a plunge 53–90°. Minor principal stress (σ_3) ranges from 6 to 10 MPa, with the direction 220° and a plunge of 0–20°.

During the preliminary phase of site investigations, the NE-1 fracture system was clearly delineated by surface and borehole geophysical methods [*Rhén et al*., 1997]. In the excavation phase, it caused significant problems due to severe water inflow (once grouted, 1600 liters per minute was flowing through an open valve on a 57 mm diameter borehole drilled into it; Figure 2 [*Rhén et al*., 1997]). Where the fracture system intersects the tunnel, three parallel branches of NE-1 are separated by less fractured host rock composed of Äspö diorite and fine-grained granite, both having been metamorphosed to a certain extent. These are referred to as NE-1-I (20 m wide), NE-1-II (12 m wide), and NE-1-III (30 m). NE-1-I and NE-1-II are separated by about 8 m of fractured host rock while NE-1-II and NE-1-III are separated by about 10 m of less fractured host rock, giving a total width of the system of about 80 m. The widths and distances given are based on our own observations during the seismic experiment using the fracture locations and markers identified by SKB on the tunnel walls. In addition, a study by *Berglund et al.* [2003] provides information on the different hydraulic properties of the individual fracture sets. The first two fracture sets (NE-1-I and NE-1-II) are described as highly fractured, partly clay altered with the latter being more hydraulically conductive then the former. NE-1-III is referred to as fractured and highly hydraulically conductive (Figure 2). Its central part is a 5–8 m wide partly clay altered zone.

Figure 2. Water inflow (1600 L/min, 57 mm diameter hole) from NE-1-III showing the significance of fracture zone delineation and characterization in the preliminary site planning stage. Photo from *Rhén et al.* [1997].

All three sets are described as water bearing with an average fracture frequency of approximately 15 fractures/m [*Wahlgren et al*., 2006]. The EW-3 zone (Figure 1) is about 12 m wide, with five different fracture sets within it with low to medium degrees of clay alteration, medium to strong tectonization, and an average fracture frequency of approximately 17/m. The central fracture set is 1.5–2 m wide with altered clay fillings [*Berglund et al*., 2003]. The whole zone represents the contact between Äspö diorite and fine-grained granite. Prior to being sealed, it leaked 90 liters of water per minute. According to *Berglund et al.* [2003], NE-1 and EW-1 (Figure 1) represent major zones of weaknesses, marking the southern and northern boundary of a block.

Aside from the two aforesaid fracture systems, another one striking mainly NE-SW, located between the NE-1 and EW-3 (Figure 1, dashed line between the NE-1 and EW-3), was also crossed by the seismic line. This fracture zone was identified in the earlier studies by *Kornfält and Wikman* [1988] and *Rydström and Gereben* [1989], but no naming or structural information on it was found by our literature studies.

3. Äspö HRL Seismic Experiment

The seismic survey at the Äspö HRL site was conducted using a combination of conventional 10 Hz vertical geophones, a seismic landstreamer [*Brodic et al*., 2015; *Malehmir et al*., 2015a], 1C wireless recorders (connected to 10 Hz vertical geophones), and 3C wireless recorders (connected to MEMS-based, DSU3™ sensors). A Sercel Lite™ acquisition system was used for data recording. Based on experience from other crystalline rock environments, a 500 kg weight-drop hammer mounted on a commercially available skid steer loader was used as the seismic source [*Sopher et al*., 2014; *Place et al*., 2015; *Malehmir et al*., 2017]. At every source location, the drop hammer was released 5 times onto a square-shaped hard aluminum plate (60 cm by 60 cm and about 2.5 cm thick) mounted at the bottom of the hammer casing. The hits were recorded within a time window of 25 s and later vertically shifted to zero and stacked together to increase the S/N. The resulting stacked source gathers were reduced to 1 s record length for further processing and analysis. Table 1 shows the main acquisition parameters of the seismic survey.

GPS-time synchronization of the seismic data was obtained by placing the recording vehicle outside the tunnel and connecting it to the tunnel seismic line via a 50 m long extension cable. Starting from about 50 m away from the entrance to the tunnel, to ensure good sensor-ground coupling, we drilled and planted 279 vertical component 10 Hz geophones (7 cm spike) at every 4 m. Geophones were vertically planted in drill holes made on the rock exposed on the side of the tunnel, 5–35 cm from the tunnel floor (labeled as Geophones I in Figures 1 and 3; also see Figure 4a). Four meters away from the last planted geophone, the

Table 1. Main Acquisition Parameters of the Tunnel-Surface Seismic Survey at Äspö HRL

Acquisition System	Sercel Lite
Total number of receivers in the tunnel	413
Planted vertical 10 Hz geophones	333 (4 m apart)
Landstreamer units	80-3C DSU3 (20 × 4 m + 60 × 2 m)
Total number of receivers on the surface	75 (51-1C 10 Hz and 24-3C DSU3)
Nominal surface receiver spacing	12 m
Recording length	25 s (reduced to 1 s after vertical stacking)
Sampling rate	1 ms
Source	Skid steer loader mounted drop hammer (500 kg)
Number of hits per source location	5
Nominal source spacing	8 m
Total number of source points	229 (tunnel and surface)

seismic landstreamer (MEMS-based, 80 DSU3 units, 200 m long) was deployed. The units were placed along the edge of the asphalt on the tunnel floor, in the continuation of the planted geophone line segment (landstreamer in Figure 3; also see Figure 4). Due to the 3C nature of the landstreamer units, it was positioned along the intersection of the NE-1 and EW-3 zones and the tunnel. In addition to these, 54 vertical component 10 Hz geophones, at 4 m intervals, were planted in drill holes at the tail of the landstreamer (Geophones II in Figures 1 and 3). The total length of the seismic spread with all different segments inside the tunnel was about 1500 m. To obtain simultaneous recording of the seismic wavefield both inside the tunnel and on the surface, another seismic line was designed using 75 wireless recorders (labeled as wireless in Figure 3). Twenty-four three-component (same type as the ones used in the streamer, DSU3™) and 51 single-component, connected to 10 Hz vertical geophones, units were deployed on the surface. Spacing between the wireless units varied from 8 to 16 m. Figure 4b shows a 10 Hz geophone planted in a drilled hole in the rock and connected to a wireless seismic recorder.

Data acquisition started in the lower tunnel part before the spiral part and advanced toward the surface with a source spacing of 4–16 m. After recording all the source points in the tunnel, the source was moved to the surface, where sources were made at all the wireless units that were accessible to the source (55 source locations). During the surface recording, data were also recorded on the seismic line inside the tunnel, and similarly, the surface receivers were recording the sources activated in the tunnel. Coordinates of all surface receivers and source positions were surveyed using a DGPS surveying system (centimeter accuracy). Inside the tunnel, known markers and their positions were used to position the receivers into the internal coordinate system used in the tunnel. These coordinates were later transformed to the same system as the surface data.

Parallel to our seismic experiment, an independent seismic survey was conducted on the sea above the tunnel, next to a small island in the central part of the site (Figure 3; marine seismic experiment arrow)

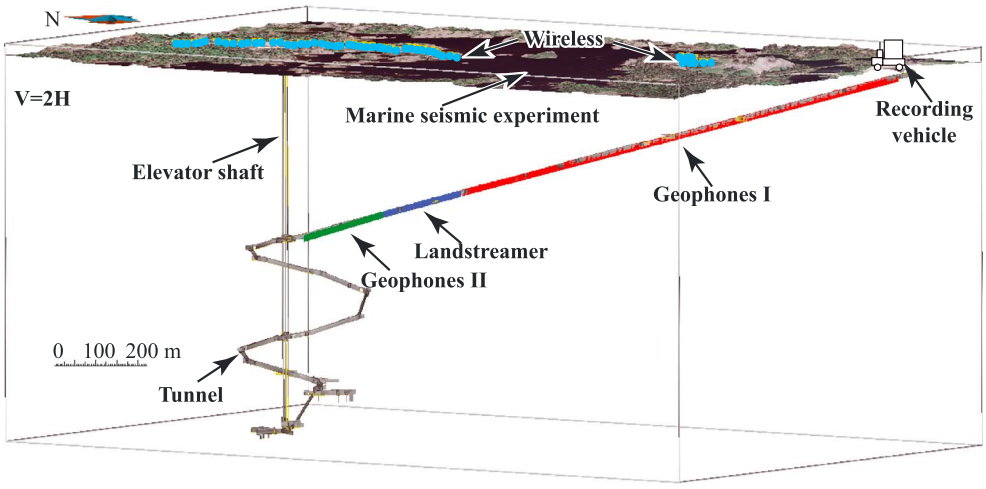

Figure 3. Tunnel model and an aerial photo projected on top of lidar (elevation) data with different parts of the seismic spread labeled and shown in different colors. Twice vertically exaggerated.

Figure 4. Examples of planted geophones in drill holes in the rock (a) in the tunnel and (b) on the surface. (c) The seismic landstreamer used in the tunnel in the downdip direction (known from drilling) of the NE-1-III fracture zone.

[see *Ronczka et al.*, 2016]. Data from four of these explosive sources were merged into our data set. Since no shooting could be done in the southern part of the line with the weight drop, these marine explosive sources partly contribute to imaging the rock mass in the southern part of the survey area.

4. Seismic Data of the Äspö HRL Site

Strong electric or electromagnetic noise is present in the tunnel and most apparent on the planted line segments (Geophones I and II in Figure 5). This noise is absent on the landstreamer data. Aside from the dominant 50 Hz electric power grid frequency, both higher- and lower-order power harmonics can also be seen. The spacing of the landstreamer units on three of the segments is 2 m, while all geophones and the units on the fourth landstreamer segment are spaced at 4 m. This irregular unit spacing results in the apparent change of slope of the direct arrivals and should not be mistaken for refracted arrivals.

Applying several notch filters corresponding to the frequencies of the individual current harmonics helped in attenuating the electric noise from the planted geophones. For the main 50 Hz current noise, a band-stop filter between 49 and 51 Hz was used, with a 2 Hz cosine taper on both sides. Aside from the electric current, noise trains coming from the southern side of the tunnel, most probably originating from the nuclear power plant located in the site's vicinity, were problematic. Vertical stacking of the repeated hits partly helped to attenuate them. However, for some records these remained quite strong, but with low frequencies and low apparent velocity. To further attenuate them, a carefully designed F-K filter was applied (Figure 6a). Inspection of Figures 5a and 6a shows observable converted and reflected events in both records, indicating that they are real features and not artifacts of the F-K filter processing.

The F-K filter was not applied to the data from the streamer or to the Geophone II part because of the steep nature of the important events likely generated from the fracture systems. Figure 6b shows an example source gather with the source being located on the landstreamer part of the seismic line, close to the edge of the NE-1 fracture system (source location 300, corresponding to receiver 300 on the seismic line). For this gather, only notch filters and the band-stop filter were applied. Note here the more distinct, more consistent, and narrower wavelets of the same events and higher-frequency content of the landstreamer units compared to the geophone segments. Comparing Figure 6a with 6b shows how the F-K filter suppresses noise coming from the side of the seismic line. This noise is more prominent in Figure 6b, but not sufficient to obscure the different seismic events of interest.

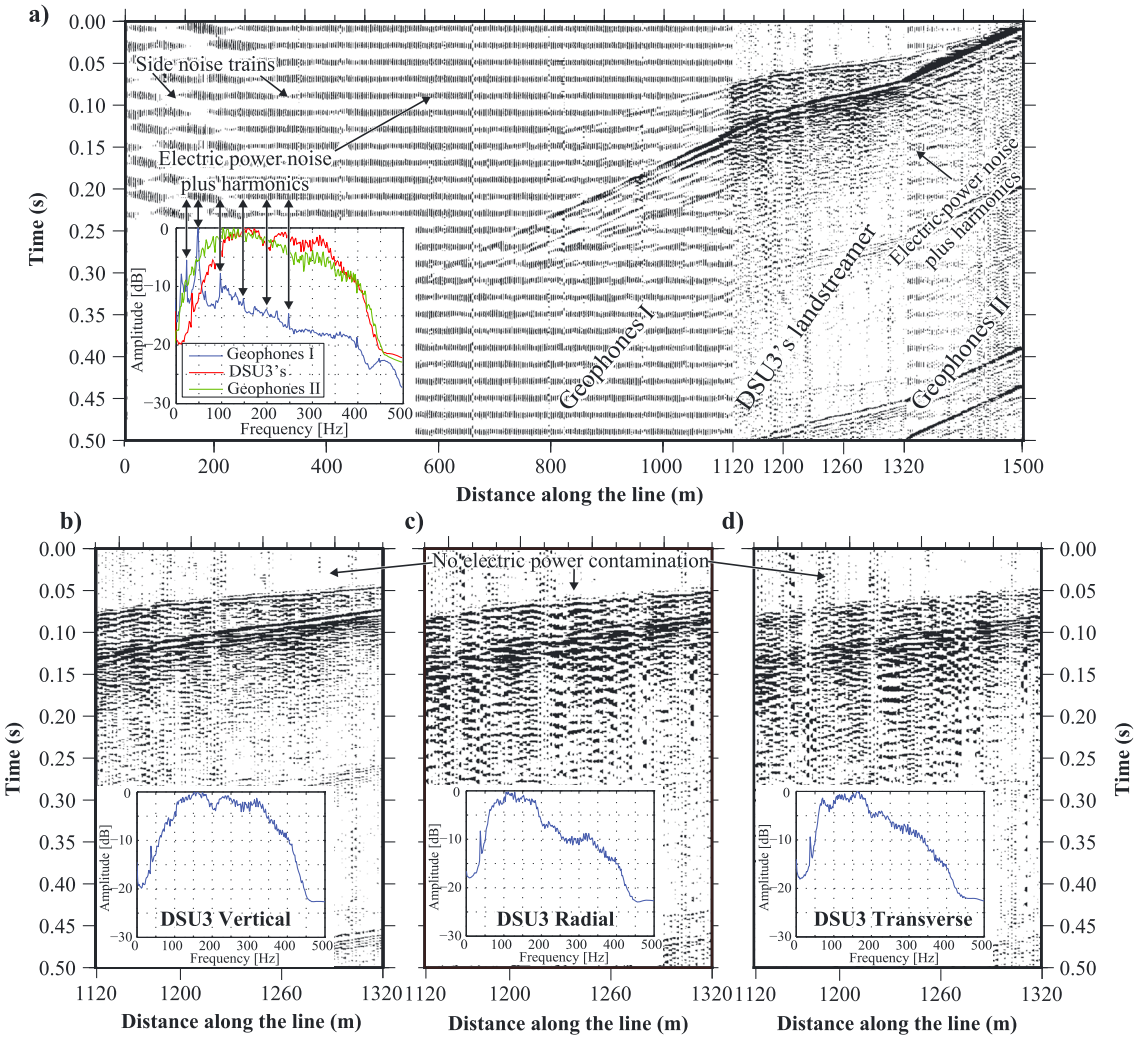

Figure 5. An example raw source gather from the seismic line inside the tunnel with trace normalization applied. (a) First 279 planted 10 Hz geophones (Geophones I), followed by 80 DSU3 unit landstreamer (DSU3's landstreamer) and 54 planted 10 Hz geophones (Geophones II), with their corresponding amplitude spectra. (b–d) An enlarged view of the data from the streamer part showing vertical, radial, and transverse components of the data, respectively, and their corresponding amplitude spectra calculated within the same window as displayed.

In addition to the source gathers shown in Figures 5 and 6, an example source gather from one of the marine explosive sources with the merged wireless and hydrophone data is shown in Figure 7a. Figure 7b shows the same explosive source simultaneously recorded on the receivers in the tunnel with some interpreted events marked. Notable are high-quality *P* and *S* wave arrivals on almost all the receivers of our seismic spread. Additionally, clear *P-S* wave mode conversion at the seafloor and both *P-S* and *S-P* conversions at the fracture system for the downgoing wavefields are observed (Figure 7b). A delay in the *P* wave first arrivals where the NE-1 fracture system is located can also be observed. Particle motion plots for receiver 280 (first unit on the landstreamer inside the tunnel) within different windows show strong vertical polarization, including *P-S* and direct *S* wave arrivals (Figure 8). This is typical for all landstreamer 3C units.

5. Seismic Imaging of the Fracture Systems

To initially characterize the rocks and fracture zones located between the tunnel and the surface we used first arrival tomography. On almost all source gathers from the tunnel the most prominent arrivals in the vertical component data are the direct shear waves (e.g., Figure 8). Strong shear waves are likely due to the large velocity contrast between the rock and the air in the tunnel, converting most of the energy to shear waves right at the tunnel floor [*Bellefleur et al*., 2004; *Malehmir and Bellefleur*, 2010]. Particle motion plots (hodograms) of the

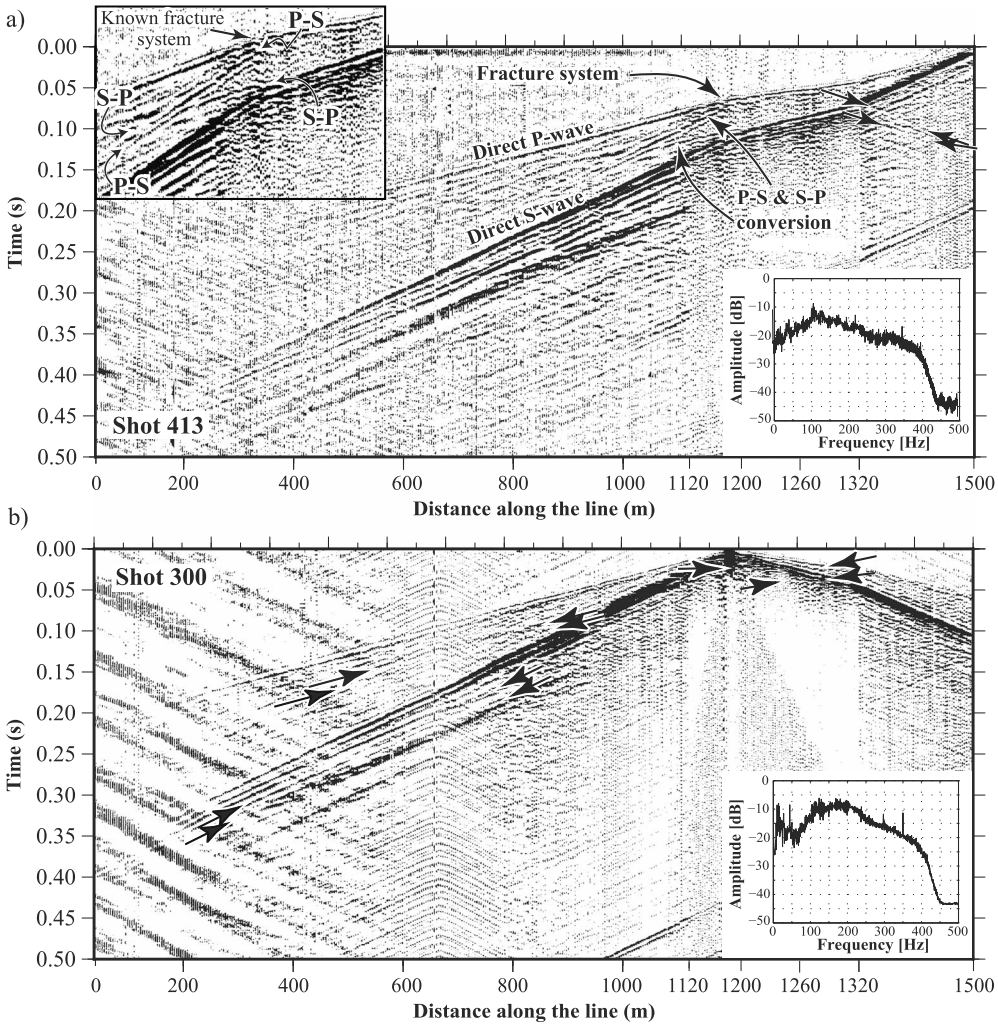

Figure 6. Example source gathers showing the quality of the seismic data after preprocessing applied. (a) Source location 413 corresponding to the last receiver (receiver 413) in the tunnel and (b) source gather for a source located at receiver 300 belonging to the landstreamer portion of the seismic line. Source location 300 is located in the zone of the NE-1 fracture system. Note the strong *P-S* and *S-P* wave modes originating from one of the known fracture zones in the tunnel, low-frequency energy at the beginning of the line, and various events marked by the arrows. The different receiver spacing of the streamer and planted geophones causes the apparent change in slope of the first arrivals.

shear wave window (Figure 8) suggest vertical polarization and no strong evidence of surface waves. Inclination of the tunnel and seismic source at an angle to vertical to the tunnel floor may have also contributed to the generation of shear waves.

Both *P* and *S* wave first arrivals from the active tunnel line and wireless recorders were manually picked. Manual picking was chosen to make sure that the delays noted on the *P* wave first arrival trend across the NE-1 fracture system were preserved (Figures 6a and 8). The picking resulted in 67,690 *P* wave and 64,540 *S* wave first arrivals from 230 sources recorded on 528 receivers, including receivers from the marine seismic experiment (40 receivers on 4 shots). Noisy traces where the arrivals could not be clearly distinguished were excluded from picking. Joint *P* and *S* wave first arrival travel time tomography was performed using the PS_tomo 3-D diving-wave tomography code [*Podvin and Lecomte*, 1991; *Hole*, 1992; *Hole and Zelt*, 1995; *Tryggvason et al*., 2002; *Tryggvason and Linde*, 2006]. Variance-based weighting of the *P* and *S* wave travel times was used for the inversion. Due to the sparse source-receiver setup on the surface and line crookedness, the tomography was done using large cells in the lateral direction. The cell sizes in the inline and depth directions were 4 m, and to obtain a 2-D model of the velocity distribution (a 2-D slice from the 3-D velocity volume), 200 m wide cells in the lateral (crossline) direction were used. Nine iterations were carried out in the

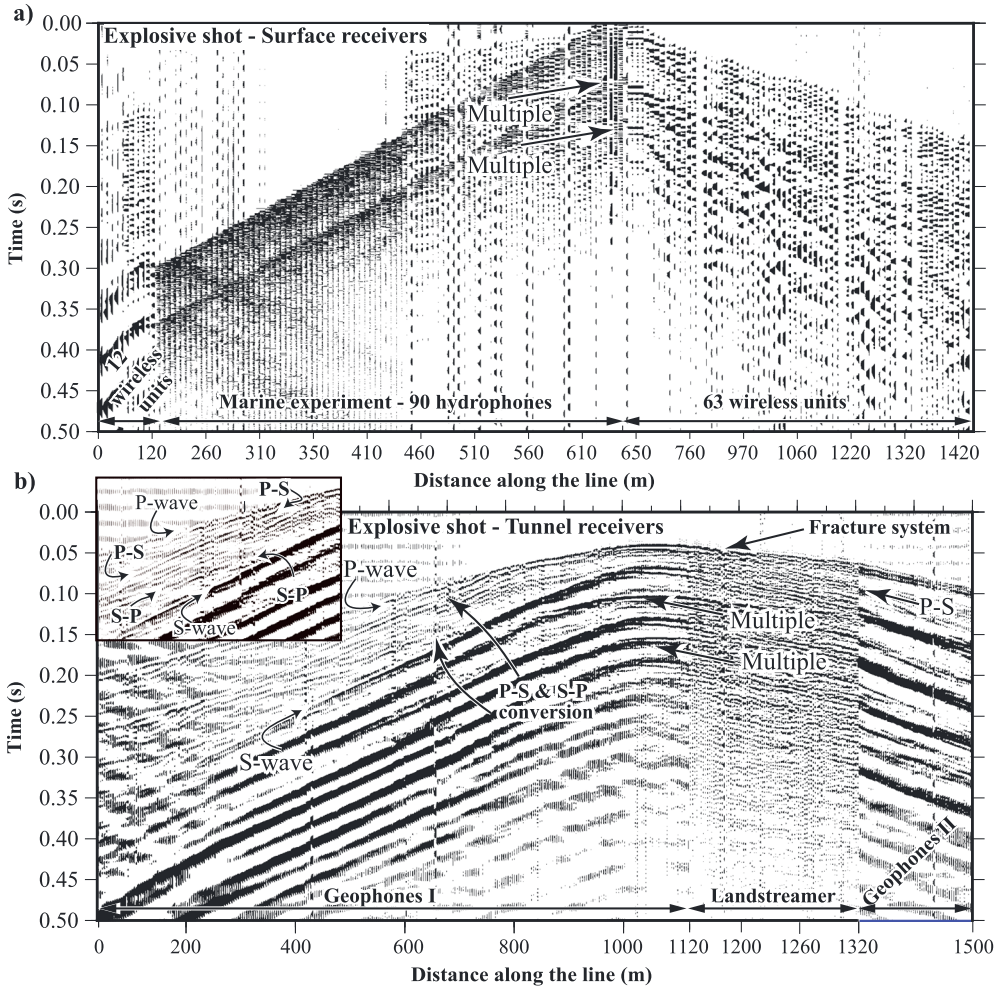

Figure 7. Example source gathers from one of the four explosive sources fired in the sea above the tunnel with (a) merged wireless and hydrophone data and (b) same explosive source simultaneously recorded by the receivers in the tunnel with certain events marked. Note the strong shear wave energy produced at the seafloor and converted back to *P* wave energy at the fracture zone.

inversion process with an RMS error of the final velocity model of 2.1 ms for the *P* and 1.4 ms for the *S* waves. Since the *S* wave tomography shows similar results as the *P* wave, to avoid redundancy, we only show and discuss the *P* wave result. Examples of first arrival picking, an overview of the distribution of all picked first arrivals, and the travel time residuals of *P* waves are shown in Figure 9.

Figure 9a also shows the three subsets of the NE-1 and less fractured and intact host rock around them (NE-1-I to NE-1-III and HR-1 to HR-4). Inspection of the source gather suggests that direct shear arrivals are less sensitive to the fracture system and show no noticeable delays on the arrival times (Figure 9a, *S* wave direct arrivals). Significant delay, however, can be noted on the *P* wave direct arrivals (Figure 9a, *P* wave direct arrivals, arrow pointing at NE-1-II zone). All arrivals align along a linear trend (Figure 9b), implying little or no refracted waves in the data and no noticeable effect of the excavation damage zone (EDZ) on the first arrivals. This is in accordance with the field situation, where even on the surface, drill holes had to be made to plant most of the geophones.

The spatial position of the EW-3 zone and its dip corresponds to a low-velocity zone seen in the *P* wave velocity model (Figures 10a and 10b). The NE-1 and NNW-3 fracture systems appear to be responsible for a complex weak zone bounded by the two and characterized by a decrease of the seismic velocities in the tomogram (Figure 10d). The velocity model shown additionally indicates a low-velocity anomaly between EW-3 and NE-1, which may be related to a minor unnamed fracture system shown in Figure 1. This fracture

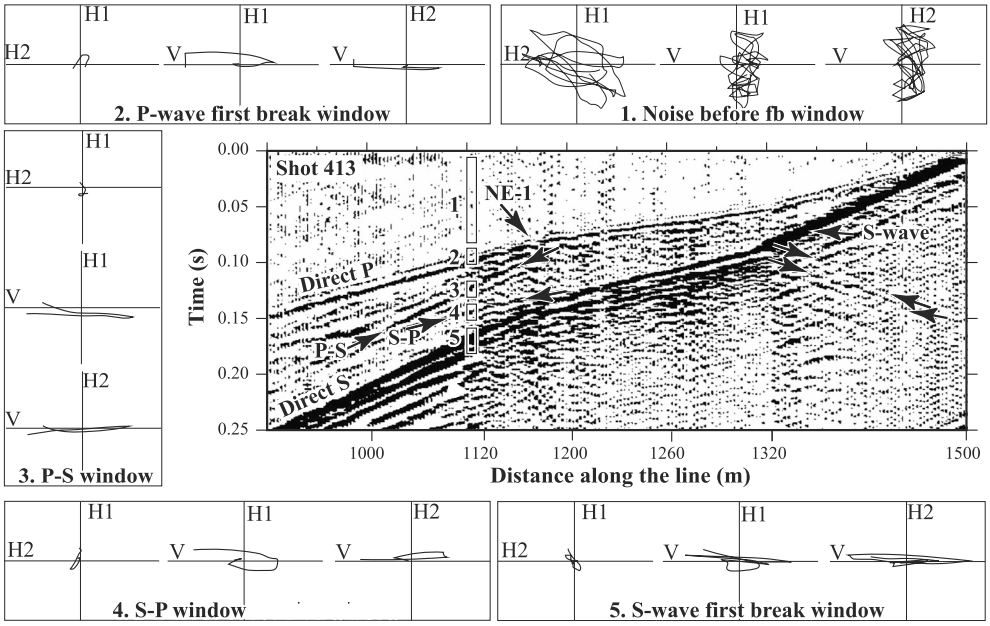

Figure 8. An enlarged view of the source gather shown in Figure 6a showing the *P* and *S* wave direct arrivals as well as features interpreted to be wave mode conversions (direct *P*-to-*S* and *S*-to-*P*) from the fracture system NE-1. Additionally, particle motion plots for different windows for receiver 280 are also shown (V: vertical, H1: radial and H2: transverse component of the landstreamer sensor). Note the delay of the *P* wave first arrivals where the NE-1 fracture system is located and strong vertical polarization for most of the events. Different gains were used for plotting particle motions to allow for better visual inspection.

system appears to change dip from the surface downward, and its intersection with the tunnel is not mapped. The low-velocity halo around the tunnel is rather an effect of the 3-D source-receiver geometry with seismic rays traveling around the tunnel (a mix of longer and shorter paths depending on source locations on the surface) squeezed into the 2-D domain during the inversion, rather than an EDZ effect [*Bohlen et al*., 2007; *Lüth et al*., 2008].

5.1. Fracture Detection and Characterization Using Wave Mode Conversions

Some surface seismic data and, in particular, borehole seismic surveys have shown that zones of high impedance contrast to the host rocks, such as fluid-filled fracture systems, ductile shear zones, and massive sulfide bodies, can increase reflectivity and generate significant amounts of *P-S* and *S-P* converted energy [*Ayarza et al*., 2000; *Bellefleur et al*., 2004; *Malehmir and Bellefleur*, 2010; *Bellefleur et al*., 2012; *Lundberg et al*., 2012; *Melanson et al*., 2015]. To provide a possible explanation of the origin of the events seen in Figures 6 and 8, two modeling approaches were used:

1. 3-D constant-velocity ray tracing travel time modeling [e.g., *Ayarza et al*., 2000] and
2. 2-D finite difference elastic modeling [e.g., *Juhlin*, 1995a].

All available information on the fracture systems in the tunnel was used as input to the modeling, such as dip angles, azimuths, width of the zones, and the average densities of the rocks hosting the fracture systems [*Rhén et al*., 1997; *Berglund et al*., 2003]. From our seismic data, we extracted apparent velocities and locations where the fractures intersect the seismic line. To obtain velocities for the fracture sets of NE-1, we analyzed data recorded on the 80 stations of the landstreamer covering it. Source gathers from the southern part of the tunnel where the arrivals could not be clearly picked were excluded, resulting in about 150 source stations being used. Furthermore, only source gathers with high S/N ratio located 200 m before, along the 200 m long landstreamer, and 200 m after it with clearly distinguishable *P* and *S* wave first arrivals were used. The landstreamer data were first divided into seven zones (NE-1-I to NE-1-III and HR-1 to HR-4) as shown in Figure 9a. Separation was done by assigning to each zone only the receivers and first arrivals belonging to that particular zone. After assigning the receivers to a particular zone, a linear regression analysis was

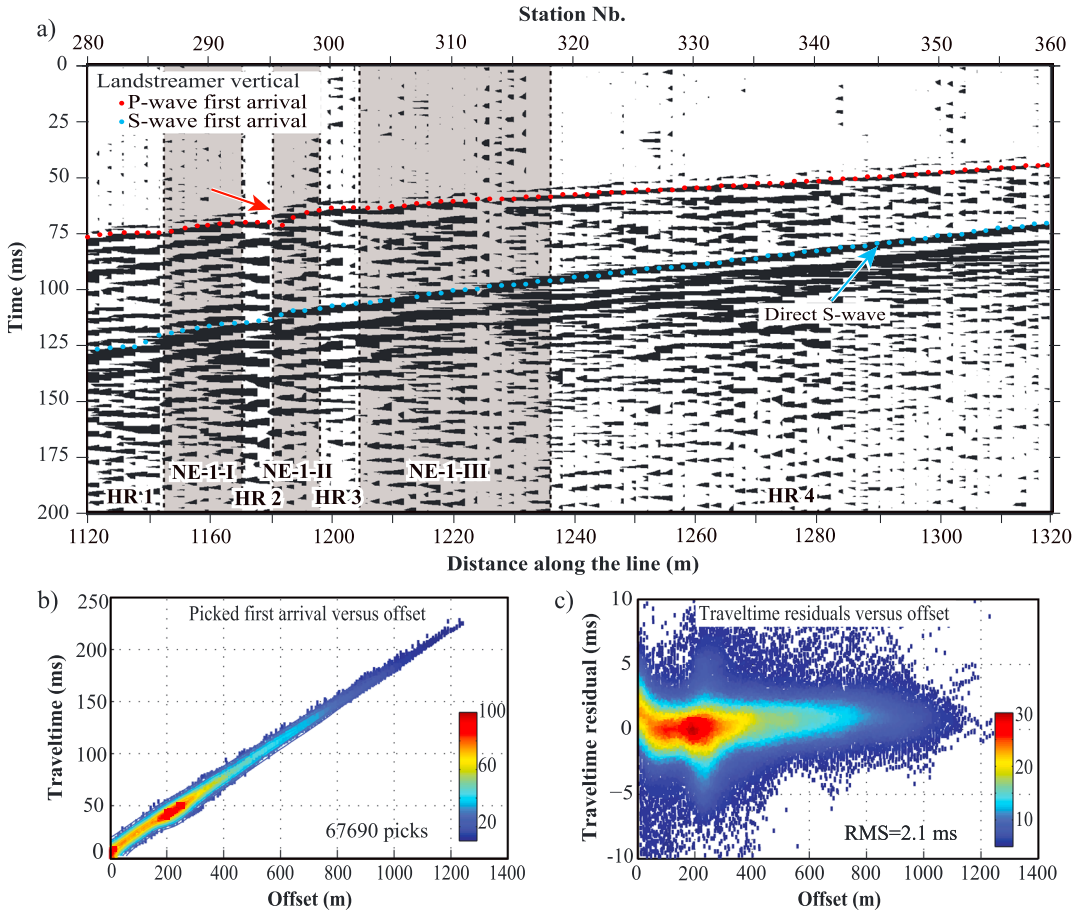

Figure 9. (a) An example of picked first arrivals of both *P* and *S* waves along the NE-1 fracture zone. Same figure shows widths and locations of different sets of NE-1 (NE-1-I to NE-1-III) and less fractured host rock separating them (HR-1 to HR-4). Locations and widths correspond to the field situation as intersected by the landstreamer in the tunnel. (b) Overview of the distribution of all *P* wave picked first arrivals and their trend with the accompanying color scale corresponding to the number of picked arrivals falling within a specific range. (c) Travel time residuals as a function of offset for the final *P* wave velocity models with RMS = 2.1 ms and color scale showing number of picks within a specific range.

performed on picked *P* and *S* wave first arrivals as a function of their offsets to obtain an estimate of the velocity for each zone. Figures 11a and 11b show a boxplot of the obtained velocities for *P* and *S* waves in the vicinity of NE-1, based on the regression analysis. Median velocities of the three NE-1 sets (NE-1-I to NE-1-III) were taken as representative of the sets for ray tracing modeling purposes. For EW-3, a median value of the differentiated travel times for the neighboring receivers located within the EW-3 zone and the same 150 sources were used to obtain an estimate of its *P* and *S* wave velocities. Near and midoffset first breaks were used as an estimate of the *P* and *S* wave velocities for the host rock further away from NE-1. Table 2 contains the geometrical information and aforesaid velocities used as input values for the two modeling approaches.

The seven zones in Figure 11 show a distinct signature on both the *P* and *S* wave velocities. Host rock HR-1 shows high velocities corresponding to the intact rock. Slightly lower velocities are seen in the host rock after NE-1 (HR-4) compared to HR-1, perhaps due to the influence of the EW-3 fracture system located at the end of the landstreamer. All zones show a decrease of velocities compared to HR-1, with *P* waves appearing more affected than the *S* waves, particularly in the HR-3 zone. Since both HR-2 and HR-3 are described as fractured host rock [*Rhén et al*., 1997; *Berglund et al*., 2003], the velocity changes within the two may indicate differences in the intensity of fracturing. Compared to fracture sets NE-1-I and III, the two mentioned host rock segments are not hydraulically conductive or mineralized [*Rhén et al*., 1997; *Berglund et al*., 2003].

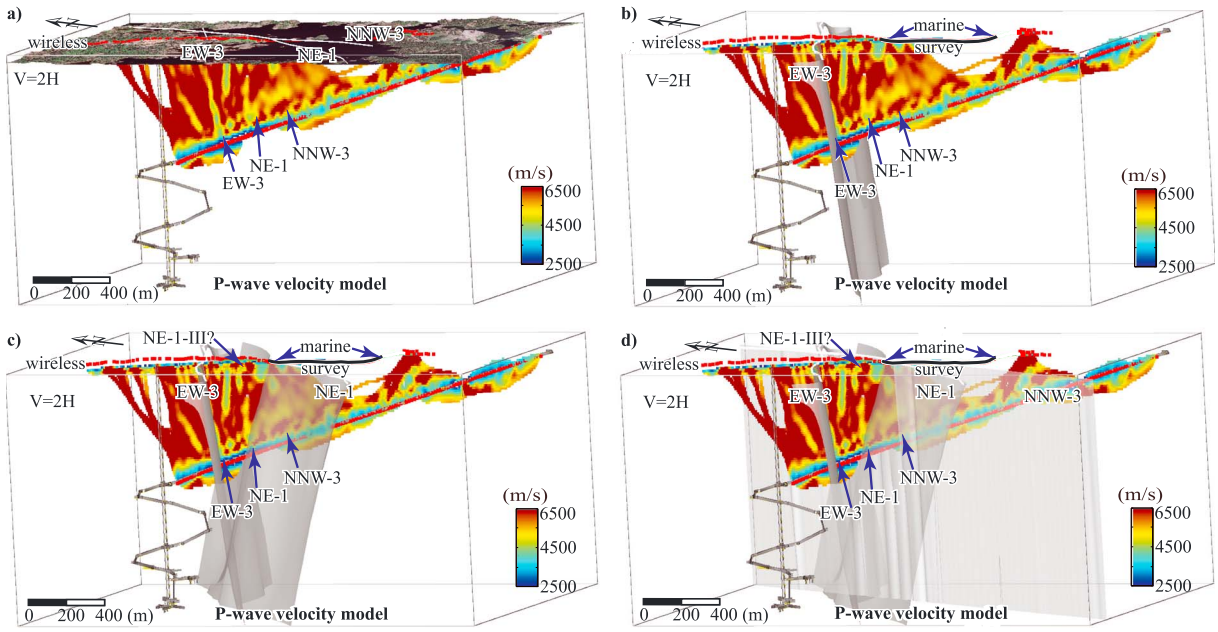

Figure 10. The 3-D view from the west of the final *P* wave velocity models obtained from joint *P* and *S* wave tomography inversion. (a) *P* wave velocity model with aerial photo projected on top of the lidar surface, tunnel model, surface projections of the fracture systems, and their intersection with the tunnel, along with location of seismic receivers both in the tunnel and on the surface shown by red dots. Same *P* wave velocity model with tunnel model, surface projections of the fracture systems, and seismic receivers and (b) EW-3 fracture zone model; (c) EW-3 and NE-1 fracture zone models; and (d) EW-3, NE-1, and NNW-3 fracture zone models shown. The *P* wave velocity model shown has both source and receiver statics applied [*Bergman et al.*, 2004; *Yordkayhun et al.*, 2009].

5.1.1. Modeling the Response of the Fracture Systems Using the 3-D Reflection Travel Time Approach

The 3-D constant-velocity ray tracing travel time modeling is based on the assumption of a homogeneous rock with a predefined constant velocity with a reflecting planar surface of known 3-D geometry within it [*Ayarza et al.*, 2000]. Commonly, a trial and error approach on the 3-D geometry is used to fit a reflection observed on a source gather (or stacked section) to a model. In our case, the geometry of the NE-1 and EW-3 fracture systems are considered known; thus, their travel time response can be calculated based on the medium velocity. Here the NE-1 fracture system consisting of three different fracture sets (NE-1-I to III zones) was modeled as a single planar reflector with velocity equal to the average of the three and dips as shown in Table 2. Host rock velocities were constant for the entire model. All aforesaid parameters were used as the model input, and travel times of all the arrivals (e.g., direct *P* wave, direct *S* wave, *P-P*, *P-S*, *S-S*, and *S-P* reflections) from the two fracture systems (NE-1 and EW-3) were calculated for the same two source locations as shown in Figure 6 (Figure 12). High-amplitude waves coming off the NE-1 fracture system corresponding to *P-S* and *S-P* converted energy show a good match between calculated direct arrivals and the real data

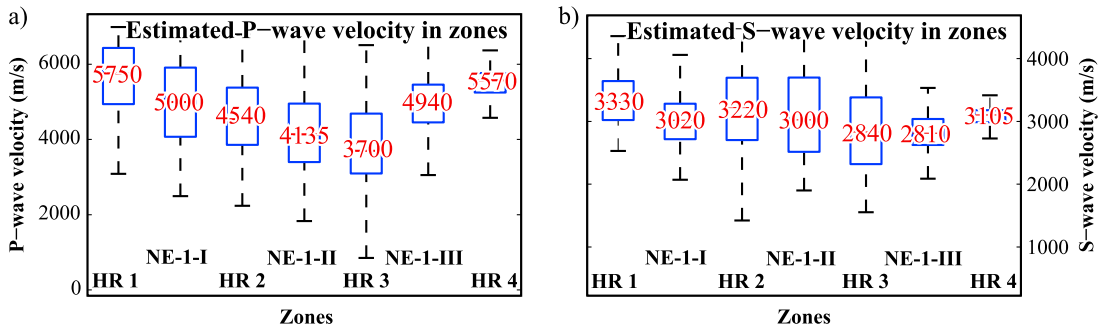

Figure 11. Estimated velocities from linear regression analysis within seven specific zones (NE-1-I to NE-1-III and HR-1 to HR-4) in the vicinity of NE-1 fracture system from (a) *P* wave and (b) *S* wave first arrivals. Only landstreamer recorded data were used and the values shown are based on approximately 150 sources with good S/N ratio. The numbers in red within boxes represent the median velocity of every zone.

Table 2. Parameters Used for Seismic Modeling

Feature	Azimuth (°)	Dip Angle (°)	Width (m)	V_p (m/s)	V_s (m/s)
Host rock	-	-	-	5650	3300
NE-1-I	231	64	20	5000	3020
NE-1-II	231	64	8	4135	3000
NE-1-III	231	64	31	4940	2810
EW-3	89	73	12	5000	3000

(Figure 12a). For EW-3, trapped energy between the two fracture systems appears to dominate near offsets (Figure 12b). Therefore, matching the events originating from the EW-3 system is based on far offsets only. The position of our seismic line makes characterization of EW-3 more complicated, since it is located where the landstreamer part of the seismic line connects to the second part of the planted geophone line (Geophones II; Figures 1 and 3).

5.1.2. Modeling the Wave Propagation Through Fracture Systems

To increase the level of confidence on the interpretation of the events shown in Figure 12a, we modeled the response of the two fracture systems for the same source location using a 2-D elastic finite difference code available in Seismic Un*x [*Juhlin*, 1995a; *Stockwell*, 1997; *Juhlin et al*., 2012]. Finite difference modeling was done assuming an isotropic media and the parameters shown in Table 2. Widths of the fracture systems and distances between individual sets were kept consistent to the field situation. To suppress additional edge

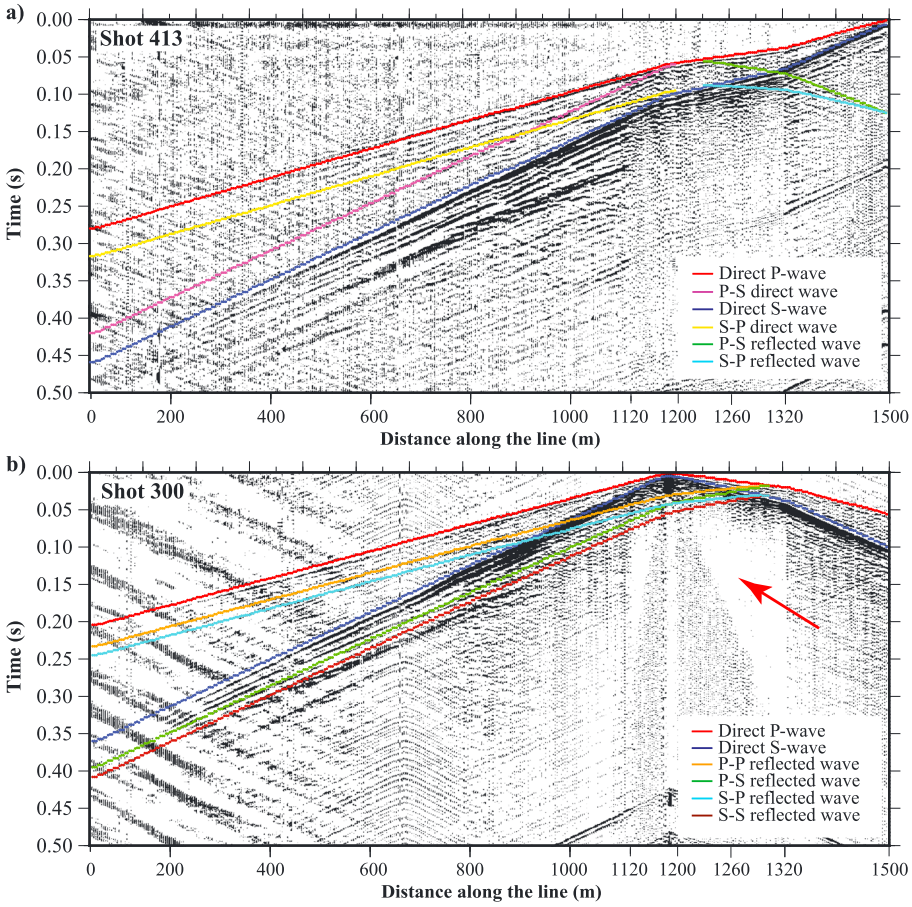

Figure 12. Results of 3-D ray tracing travel time modeling for fracture systems NE-1 and EW-3. (a) Source gather showing modeled travel times for corresponding events as shown in Figure 6a. (b) Result of travel time modeling for the EW-3 fracture system and events shown in Figure 6b. Note the damped amplitude zone (red arrow) due to trapped energy between the two fracture systems. For plotting purposes, trace normalization was applied.

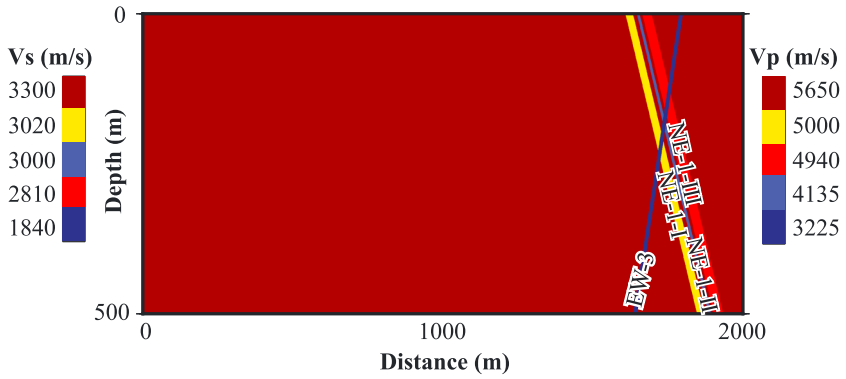

Figure 13. Velocity model used for 2-D elastic finite difference modeling. The velocities shown here are the same ones as used for 3-D travel time modeling. Over the entire model, the density was kept uniform.

effects, apparent velocities of the host rock shown in Table 2 were used as velocities of host rock segments (HR-1 to HR-4) separating the fracture sets of NE-1. A uniform density of 2755 kg/m^3 was used for the entire medium, corresponding to the average of the densities of all the rock types mapped in the northern part of the tunnel [*Rhén et al*., 1997]. For the isotropic case, the code calculates the C_{11} and C_{55} Voigt elastic stiffness. To include the fracture systems (Figure 13), a percentage decrease of each of the elastic stiffness within the zones where the fracture systems are located was calculated to match the parameters shown in Table 2. Conceptually, the model was made assuming that its top represents the tunnel floor where the seismic receivers were placed.

Since the data show quite a broadband frequency character (Figure 6), a Ricker wavelet with a dominant frequency of 180 Hz was used to generate synthetic seismograms. To prevent numerical artifacts, a grid cell size of 1 m in both the vertical and the horizontal directions was used. A free surface boundary condition was applied at the top and absorbing boundary conditions on the model sides to avoid strong reflections off the model boundaries. Intrinsic attenuation was not included ($Q = \infty$). The calculated travel times using the 3-D ray tracing approach correspond well to both the real and synthetic source gathers (Figure 14) with a good match of the modeled responses with those observed on the real source gather as shown in Figure 14c. Strong scattering from the edges of cells as seen in Figures 14a and 14b is a consequence of the way the fracture zones were introduced into the model. Nevertheless, it is not so strong as to obscure the recognition of the events of interest.

5.2. Dynamic Elastic Properties of the Fracture Systems

Subsurface elastic property estimation is essential for engineering purposes, reducing drilling and mining risks, maximizing oil and gas reservoir productivity, or understanding crustal stresses driving tectonic processes. Based on how they are determined, the elastic properties of materials can be classified into static and dynamic ones. By definition, the static moduli are obtained directly in deformational (stress-strain) experiments, while the dynamic ones are calculated from the seismic velocities and density [*Mavko et al*., 2009; *Meléndez-Martínez and Schmitt*, 2016]. Unless conducted on an ideally elastic material, the calculated value of the dynamic moduli and measured static ones will differ, with the dynamic ones generally indicating more competent rocks. The difference between the two can be related to the different strain (deformation) amplitudes involved in static measurements and those caused by a passing seismic wave (about 10^{-3} and 10^{-6}, respectively) [*Barton*, 2007; *Mavko et al*., 2009]. Additionally, the presence of cracks, joints or pores, and their fluids play an important role [*Blake and Faulkner*, 2016]. Regardless of the differences between the two, the dynamic elastic properties for the NE-1 fracture system, namely, V_p/V_s and Poisson's ratios, were estimated to test if the highly permeable fracture sets of NE-1 show distinct signatures. To obtain the ratios, two approaches were used. According to *Geldart and Sheriff* [2004], the V_p/V_s ratio can be approximated as the travel time ratio of *S* and *P* wave direct arrivals, t_S/t_P picked on the same receiver. For this step, we used the same 150 sources and 80 landstreamer stations as used for obtaining the velocities shown in Figure 11. The values obtained using the travel time ratios are influenced by all the rock a seismic wave

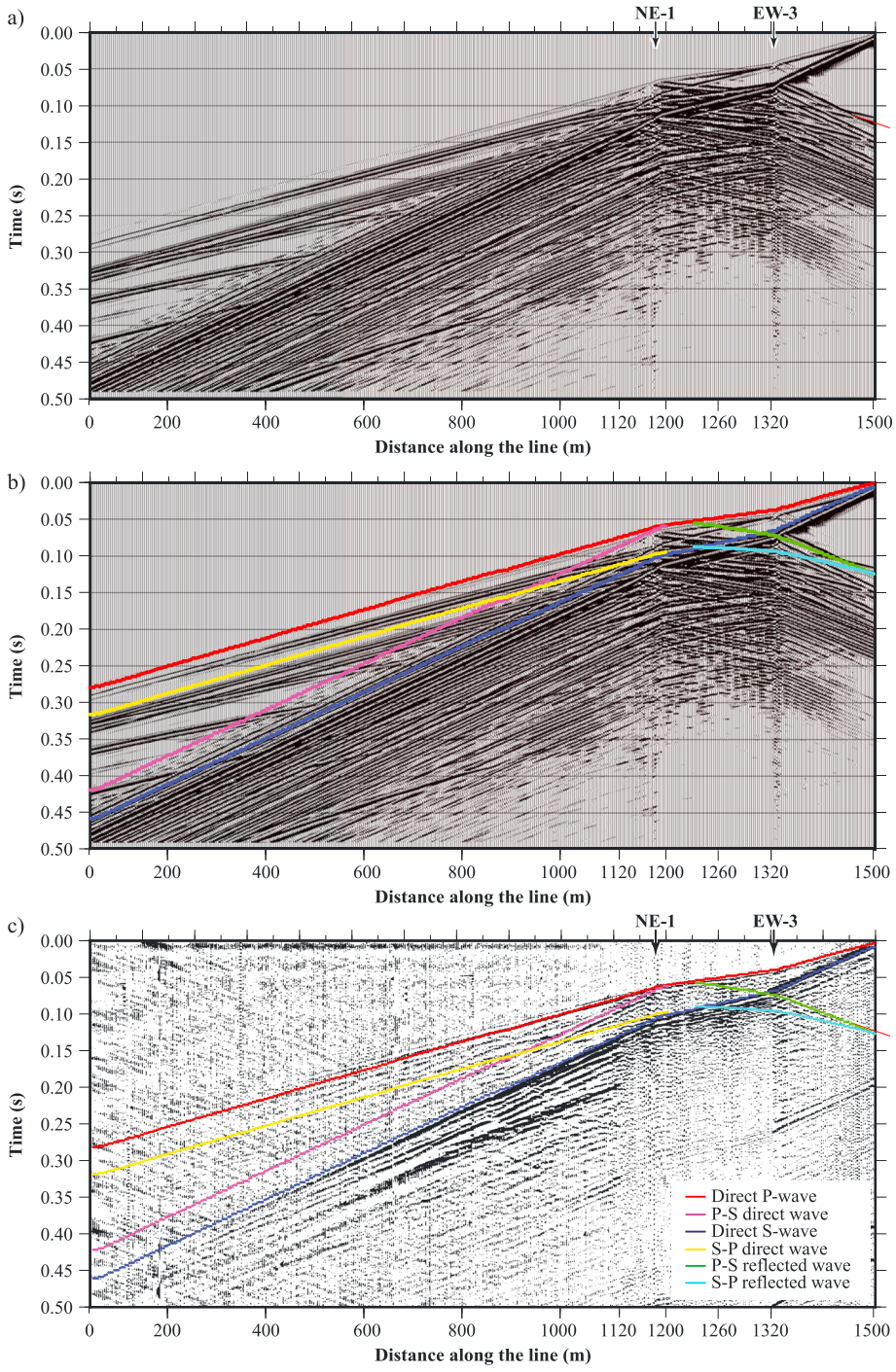

Figure 14. (a) Synthetic seismograms generated using the 2-D elastic finite difference modeling approach with arrows showing the location of the corresponding fracture systems. (b) Same seismograms with superimposed travel times from the NE-1 fracture system modeled using the 3-D ray tracing approach and the direct *P* and *S* wave velocities. (c) Real data source gather with calculated travel times superimposed.

encountered along its propagation, hence corresponding to the path average ratio. In the second approach, to obtain a more focused and local analysis, the velocities shown in Figure 11 were used to calculate V_P/V_S and Poisson's (σ) ratio for the seven zones in the vicinity of NE-1. The Poisson's ratio (σ) was calculated using the isotropic case formula [*Geldart and Sheriff*, 2004]:

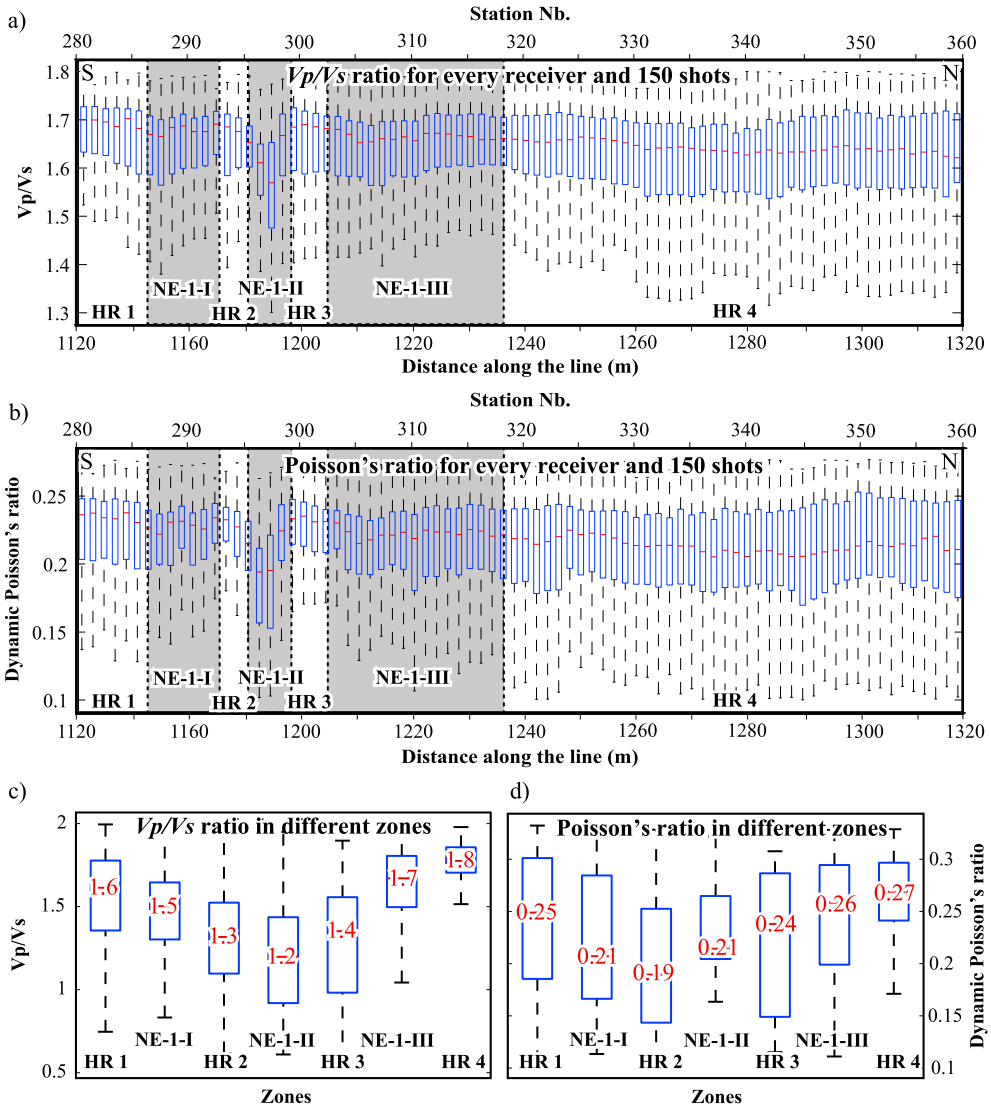

Figure 15. Variations of dynamic elastic properties in the zone of the NE-1 fracture system calculated using two different approaches. (a) V_p/V_s ratio variation and (b) Poisson's ratio variation based on the ratio of picked first arrivals of the *S* and *P* waves from 150 sources along a portion of the seismic line in the tunnel. (c) V_p/V_s ratio variation and (d) Poisson's ratio variation within seven different zones as shown in Figure 9 and velocities obtained from regression analysis. HR represents host rock before and after NE-1 (HR 1 and 4) and between its different sets (HR 2 and 3).

$$\sigma = \frac{(Vp/Vs)^2 - 2}{2\left[(Vp/Vs)^2 - 1\right]} \tag{1}$$

Figures 15a and 15b show boxplots of V_p/V_s and Poisson's ratio calculated using the travel time ratios of the picked *S* and *P* wave direct arrivals (t_S/t_P), while Figures 15c and 15d show the variation within the seven different zones based on using the velocities in Figure 11. Red lines and numbers inside blue boxes bounded by the first and third quartiles depict the median value per zone. Individual fracture sets of NE-1 are marked with NE-1-I to NE-1-III and the host rock separating them with HR-1 to HR-4. Even though seismic wavelengths are estimated to be on the order of 20–25 m, the fracture system still produces a distinct seismic signature as seen on the source gather shown in Figures 8 and 9. The most prominent decrease can be seen in the portion of the NE-1-II fracture set, with a distinct drop of all parameters (Figure 15). According to the hydraulic conductivity description by *Rhén et al.* [1997] and *Berglund et al.* [2003], this may indicate a transition from a high fluid conductivity to a non or low-conductivity environment. The distinct drop of the parameters spatially coincides

with the *P-S* and *S-P* wave mode conversions seen both in the real data and supported by the modeling studies. Considering the seismic wavelengths, size, and position of the NE-1-II, this marked decrease is likely an average over the fracture set and the more competent host rock separating it from the NE-1-III and NE-1-I.

5.3. Seismic Quality Factor *Q* of Fracture Zones

Seismic attenuation, in the most general sense, represents the loss of energy or amplitude of a seismic wave as it propagates through a medium [*Knopoff*, 1964; *Sheriff*, 2002]. It has been a topic of research for almost 40 years now, and different attenuation mechanisms have been proposed [*Johnston et al.*, 1979; *Kjartansson*, 1979; *Toksöz et al.*, 1979; *Holliger and Bühnemann*, 1996; *Wang*, 2008; *Ekanem et al.*, 2013]. Attenuation involves loss of energy due to geometrical spreading, scattering, and anelastic or intrinsic attenuation resulting from grain boundary friction or fluid movements [*Johnston et al.*, 1979; *Mavko et al.*, 2009]. Knowledge of the attenuation is important since it can provide insight into the intensity of fracturing, lithology, and porosity or indicate hydrocarbons in reservoir characterization [*Kjartansson*, 1979; *Dasgupta and Clark*, 1998; *Xu and Stewart*, 2006; *Wang*, 2008]. To quantify to what extent the different hydraulically conductive sets of the NE-1 fracture system influences the attenuation of passing seismic waves, we calculated *Q* within the same zones as used for the calculation of the velocities (Figure 11) and dynamic mechanical parameters (Figure 15). According to *Tonn* [1991], the *Q* value can be estimated as the amplitude ratio of the same seismic event recorded by two receivers located at distances x_1 and x_2 using

$$Q = \frac{\omega \Delta x}{2c}\left[\ln\left(\frac{A(x_1)}{A(x_2)}\right)\right]^{-1}, \tag{2}$$

with $A(x_1)$ and $A(x_2)$ being the amplitudes at two receiver locations, c the velocity, and $\omega = 2\pi f$ the dominant angular frequency. For the purpose of our study, we assume that *Q* is frequency independent in the frequency range of our data. To calculate *Q* based on the amplitude decay method, the same 150 source gathers and 80 receivers were used after a geometric spreading correction had been applied using the source-receiver offsets as the scalar. Noisy traces and traces with offsets less than 80 m (to suppress source-induced noise) were excluded from the analysis. For every source gather, we extracted data within a 10 ms window around the *P* and *S* wave direct arrivals (3 ms cosine taper on both ends). Extracted data were then subdivided by receivers located inside each of the seven zones as used for calculation of velocities shown in Figure 11. Within the zones, natural logarithms of the peak amplitude of every receiver were calculated, and as function of offset, used as the base for linear regression analysis (Figure 16). A minimum of four stations per zone was used for the analysis (Figure 16). Offsets from the source positions were used as distance (Δx in the formula) within each of the seven individual zones and the slope of the line from the previous step used to calculate average *Q* [*Juhlin*, 1990; *Tonn*, 1991; *Juhlin*, 1995b]. This was done for both *P* and *S* wave direct arrivals with dominant frequencies of 180 Hz and 160 Hz, respectively. For every zone, the median velocities shown in Figure 11 for zones HR-1 to HR-4 and NE-1-I to NE-1-III were used to calculate *Q* (Figure 17).

Q values within and around NE-1-II are quite low, suggesting the zone and neighboring rocks to be highly attenuating. Other regions of the host rock show a higher *Q* value, implying more competent rocks. The hydraulically conductive set of NE-1 (NE-1-III) shows high *Q* values compared to the other sets and the HR-1 segment. The *S* wave attenuation shows a similar pattern, with NE-1-III being less attenuating compared to other sets or the fractured host rock segments separating them. Since the final results of the *Q* estimates are shown as a boxplot (Figure 17), no norm of residuals or standard errors are shown to avoid redundancy.

6. Discussion

6.1. Surface-Tunnel-Surface Velocity Tomography

Studies involving tunnel-to-surface experiments have previously been reported by *Gritto et al.* [2003, 2004]. Compared to them, the study presented here was done with simultaneous data recording on the surface and inside the tunnel, allowing better spatial coverage for the travel time tomography. The velocity model shown in Figure 10 was forced to be 2-D (wide crossline cell of 200 m), although a 3-D inversion was performed and a 3-D source-receiver setup was used for travel time calculations; hence, its interpretation should be viewed with certain caution. An attempt to do a 3-D inversion of the first arrivals was made using a grid size of 12 m in the crossline direction, which resulted in numerous gaps in the inverted velocity model, making the interpretation of the results difficult. To ensure that features in the velocity models are not inversion

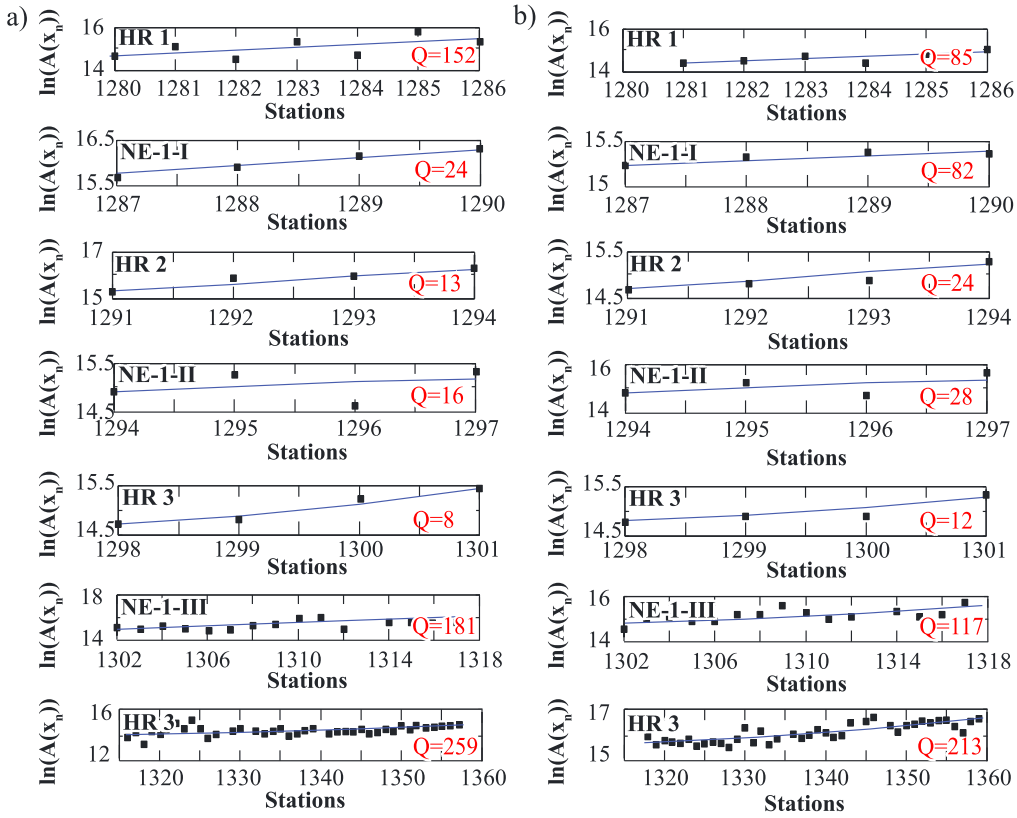

Figure 16. An example of linear regression fitting to the peak amplitudes of the receivers within the seven zones and a 10 ms tapered window around picked first arrivals. (a) *P* and (b) *S* wave example. *ln*(A(x_n)) represents the logarithmic value of the amplitude of the corresponding station.

artifacts, we tried to perturb the picked first arrival travel times by adding a series of randomly generated travel times with a mean value of ±3 ms [*Malehmir et al.*, 2015b]. This did not significantly influence the result, with the anomalous zones still being preserved. Additional tests of the initial model perturbation, and a test of possible errors introduced by the coordinate transformation from internal coordinate system in the tunnel to the one used [*Maurer and Green*, 1997; *Malehmir et al.*, 2015b], was based on adding a randomly generated series of ±0.5 m (mean value) to the receiver coordinates and reinverting this new data set. Again, no major change was seen in the final velocity model.

The northern part of the line has good data coverage, so the velocity anomalies related with the NE-1 and EW-3 systems could still be reasonably well resolved. Significant improvement and more spatially constrained

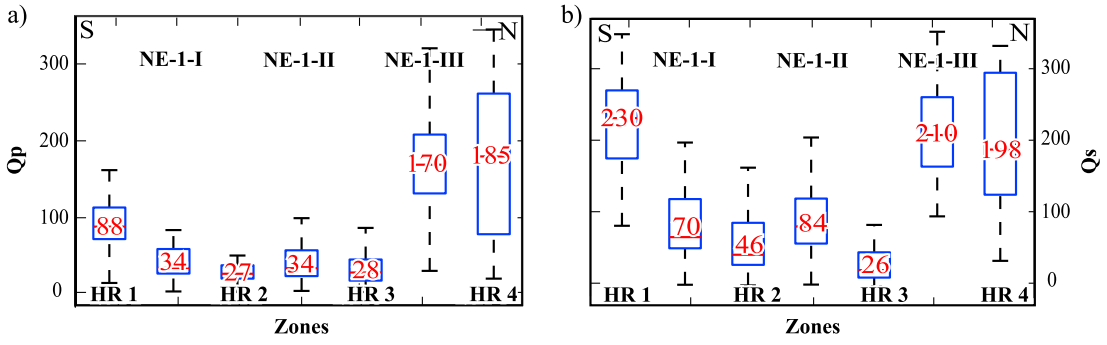

Figure 17. Seismic quality factor *Q* across the NE-1 fracture system obtained using the amplitude decay method on (a) *P* wave direct arrivals and (b) *S* wave direct arrivals. To calculate the *Q*, median velocities of all zones shown in Figure 11 were used. The red numbers inside the box represent the median value of *Q* per zone.

low-velocity anomalies related to the fracture systems were obtained with the joint inversion than with inverting only for *P* wave arrivals. In the case of EW-3, the number of source and receiver pairs, and their spatial positions favor the imaging of the fracture system itself (Figure 10b, EW-3 arrow). The fracture models extracted from the SKB database confirm that this velocity decrease spatially corresponds to the EW-3 system. Low-velocity anomalies that follow the dip of NE-1 can be seen in the velocity model, but constraining their lateral extent based only on the tomography result remains uncertain. Additional complexities in interpreting the velocity anomalies related to NE-1 are introduced by the presence of the NNW-3 fracture zone. A low-velocity zone having its root where the NE-1 crosses the tunnel and continuing upward with opposite dip is also present on the *P* wave velocity model (Figure 10c, arrow NE-1-III). This low-velocity zone may be connected with the NE-1-III fracture set of the NE-1 zone that appears to change its dip angle above the tunnel intersection. Surface projection of this low-velocity region corresponds to a lineament seen on the aerial photo, supporting the claim that this zone is rather a geological feature than an inversion artifact (Figure 10a, NE-1-III arrow). The modeling studies of *Berglund et al.* [2003] also conclude that the NE-1 zone appears to change its dip angle from the surface downward. Another consistent zone where the velocities decrease in the velocity model can be seen following the EW-3 (Figure 10, velocity decrease after EW-3 in the downdip direction).

6.2. Seismic Signature of the Fracture Systems

Lack of a significant decrease in the *S* wave velocity over the NE-1 zone (Figures 8 and 11) may be an effect of the preferred fracture orientation within the zone. Open fractures may be controlled by the original development of the fracture system and aligned parallel to the dip or they may be controlled by the stress field, giving rise to extensive-dilatancy anisotropy [*Crampin*, 1981, 1987; *Yardley and Crampin*, 1991]. Cracks aligned parallel to the dip of the fracture system, either original or due to the current stress field, would favor the delay of *P* waves over *S* waves propagating across the system. For an *S* wave as shown in Figure 8, with cracks aligned parallel to the dip angle of the fracture system and assuming that it is radially polarized (particles polarized parallel to the plane of cracks), no significant effect on its propagation would be observed [*Anderson et al*., 1974].

Studies have reported that fully fluid saturated fracture zones will tend to have lower seismic velocities and possibly higher hydraulic conductivity [*Juhlin*, 1995b]. High hydraulic conductivity may increase the pore pressure, hence reducing the effective stresses further decreasing the velocities, increasing attenuation, and making the fracture effect more pronounced [*Dvorkin et al*., 1999; *Siggins and Dewhurst*, 2003; *Wang et al.*, 2012]. However, only a small decrease of velocities in the highly hydraulically conductive NE-1-III zone indicates the opposite to be the case. Whether this effect is due to mineralization of the fractures, fracture intensity, apertures of the cracks and fractures, presence of clays and clay alteration, or due to grout in the fractures remains uncertain. Changes to the nature of the zone due to the grouting cannot be ruled out. The seismic waves may not be sampling the unaffected portion of the zone.

A significant amount of *S-P* mode converted energy is associated with the NE-1 fracture system. We can note that the *P-P* and *S-S* reflected waves are difficult to identify in the real data, while the *P-S* and *S-P* mode converted direct and reflected waves are clearly present (Figure 12a). Considering the spatial location of the mode conversions of the direct *P* and *S* waves, we argue that the mode conversions are related to the transition between the highly hydraulically conductive portion of the NE-1 fracture system (NE-1-III) and its low hydraulically conductive neighbor NE-1-II and fractured host rock segments HR-2 and HR-3. Accounting for the wavelengths of our data set (20–25 m), it is likely that the mode conversions are a cumulative effect of the mentioned zones. To obtain a more constrained interpretation, other information would be required, such as, e.g., full-waveform sonic borehole logging. The nature of the direct *S-P* mode conversions observed in the data and the delays in the *P* wave first arrivals (Figure 8) still remain uncertain. *Hardage et al.* [2011], for example, argue that, in the case of aligned fractures, increased fracture density could noticeably decrease velocity of a *P* wave propagating normal to the fracture plane, while the radially polarized shear wave velocity remains the same. Even though this argument supports our observation, it does not explain why strong *P-S* conversion occurs at the zone. The mode conversions and delays are likely a joint effect of the different density, spacing, apertures of the cracks and fractures, and their alignment, which in return influences the hydraulic conductivity of the fracture sets [*Anderson et al*., 1974; *Hardage et al*., 2011]. The EW-3 fracture system is less hydraulically conductive (90 L/min prior to grouting) and relatively narrow

(12 m), and no noticeable *P-S* and *S-P* direct wave conversions from it are seen in the data. The energy trapped between the two fracture systems (red arrow on Figure 12b) makes the interpretation of the EW-3 exact location in the source gathers a difficult task due to noise masking all the reflected arrivals at near offsets. Nevertheless, far offset events on the real data appear to match relatively well with the calculated travel times (Figure 12b).

The finite difference elastic modeling result shown in Figure 14 was done in 2-D assuming the tunnel bottom as the top of the model. Taking into account the tunnel shape and seismic sources and receivers along it, the 2-D assumption may be valid for modeling of the shallow events originating from the boundaries of the fracture systems. If deeper structures are to be imaged, or the contact of NE-1 and EW-3, 3-D modeling should provide more accurate results, where the dip of the two, along with their widths, should be used as the model input. One drawback of the modeling strategy of introducing the fracture systems in the code was more "edge effects" due to sharp changes of the neighboring cell properties. Even with the severe scattering seen in the results, important information was obtained that allowed us to partly reconstruct the delay of the *P* wave first arrivals seen in the real data and fully reconstruct the *P-S* and *S-P* mode conversions. A good match with the real data can be noted, indicating proper selection of the modeling parameters shown in Table 2.

6.3. Dynamic Elastic Properties and Seismic Attenuation Estimation

The most distinct variation in the dynamic elastic properties is over the NE-1-II fracture set (Figure 15), particularly indicated by a marked decrease in V_p/V_s. The NE-1-I fracture zone also shows a decrease in V_p/V_s and Poisson's ratio, but not as clearly as NE-1-II. The highly hydraulically conductive NE-1-III set shows an increase in the Poisson's ratio, compared to those subsets that are not highly water bearing. These variations may be due to changes in the fracture intensity and hydraulic conductivity, which in turn influence the fluid pressure and effective stresses within the fracture sets [*Dvorkin et al*., 1999; *Carcione and Cavallini*, 2002; *Siggins and Dewhurst*, 2003; *Wang et al*., 2012]. Considering the estimated accuracy of the first break picks (±1–2 ms), the calculated velocities in the fracture sets are somewhat uncertain. However, given the width of the individual fracture sets, the more intact host rock separating them, and the seismic wavelengths, we suggest that the values shown in Figure 15 are slightly underestimated and represent average values of the fracture sets and the host rock separating them. Nevertheless, the three fracture zones appear to give a clear signal in the seismic data and estimated dynamic elastic properties. The lower *S* wave velocity in NE-1-III compared to the other two (Figure 11) suggests that this zone is more fractured, and therefore more water bearing.

Compared to single-fold VSP studies [e.g., see reviews by *Tonn*, 1991; *Toverud and Ursin*, 2005], the data in this study involved the analysis of 150 source gathers around the fracture systems. Although *Q* values in certain zones shown in Figure 17 are calculated based on only four receivers, the amount of data used for the calculations provides a rough estimate of *Q* within each zone. The higher *Q* values within the zones are in the range of those observed for granites and diorites [*Knopoff*, 1964; *Badri and Mooney*, 1987; *Barton*, 2007]. The low hydraulically conductive sets of NE-1 (NE-1-I and NE-1-II) show low *Q* values for *P* and *S* waves. Compared to the intact rock, the lower *Q* values within these two fracture sets are expected and show similar characteristics to faults investigated by *Harris et al.* [1997] and *Worthington and Hudson* [2000]. The NE-1-III set, on the other hand, shows a high *Q* value for both *P* and *S* waves (Figure 17). *Pyrak-Nolte et al.* [1990], based on lab analysis of fractured rock samples, concluded that at 30 MPa confining pressures (pressures of the in situ seismic studies), the *Q* factor of high water-bearing rocks is higher than those that are less water-bearing. Hydraulic conductivity, along with clays or other minerals in the cracks of NE-1-III, may have additional effects on *Q* [*Boadu and Long*, 1996; *Rubino and Holliger*, 2012; *Kong et al*., 2013]. Both segments of the host rock before and after the NE-1 system show high *Q* values (HR 1 and HR 4 in Figure 17), indicating a less attenuating environment and more competent rocks. *P* wave attenuation within the HR 1 zone is higher than HR 4, possibly due to the number of stations used for linear regression purposes (HR 1 is calculated using 7 receivers, while HR 4 included about 40 receivers; Figure 16). Both *P* and *S* wave results in Figure 17 show low values in the two host rock segments (HR 2 and HR 3) separating NE-1-II from its neighboring sets. These results indicate less intact and fractured rocks, also consistent with previous studies [*Rhén et al*., 1997; *Berglund et al*., 2003]. Generally, the *P* wave appears more attenuated than the *S* wave, supporting the idea that preferred fracture orientations are highly influencing the wave speeds.

In summary, the two less hydraulically conductive zones have lower V_p/V_s and Poisson's ratio than the more conductive NE-1-III zone. These zones also have lower *Q* values (Figure 17). Combined, these observations

suggest that NE-1-I and NE-1-II are of a different nature than NE-1-III and their seismic signature can be used to characterize them.

7. Conclusions

A surface-tunnel-surface seismic experiment was conducted at the Äspö Hard Rock Laboratory in southern Sweden with sources and receivers both in the tunnel and on the surface. First arrivals from all sources and receivers were manually picked and used for joint *P* and *S* wave travel time tomography. The obtained *P* wave velocity model shows low-velocity zones that correlate relatively well with the locations and dip angles of the NE-1 and EW-3 fracture systems investigated in this study. Additionally, minor fracture systems appear as low-velocity anomalies. Some of these minor fracture systems observed in the velocity model were mapped in previous studies and others are new in this study.

Inspection of source gathers shows that the NE-1 fracture system generated significant mode-converted direct and reflected *P* and *S* wave energy. The 3-D ray tracing reflection travel time modeling was performed to verify these observations. It was illustrated that the fracture system was responsible for generation of *P-S* and *S-P* reflections. The EW-3 zone has a smaller spatial extent and is less hydraulically conductive than parts of the NE-1 system, and for this fracture system, all reflected and mode-converted waves were modeled using the same approach. The modeled travel times for EW-3 show a reasonable match between the events seen in the source gathers and the ones modeled, at least at far offsets. The velocities extracted from the seismic data were used to further model the response of the two fracture systems using a finite difference elastic modeling method. This modeling suggests that *P-S* and *S-P* energy conversion from the two is possible, and synthetic seismograms show a good correspondence to real source gathers, and the travel times calculated using the ray tracing approach.

The NE-1 fracture system causes noticeable delays in the *P* wave first arrivals for the seismic receivers located across it in the tunnel. These delays were used as a basis for the estimation of dynamic mechanical parameters of the fracture sets, namely, V_P/V_S and Poisson's ratio, and the variation of these parameters across the fracture sets. The variation was correlated to different degrees of fluid conductivity of the different fracture sets of the NE-1 system. Estimation of the seismic *Q* factor shows that the fractures with different degrees of hydraulic conductivity show different attenuation characteristics. The low or nonhydraulically conductive fracture sets of NE-1 are highly attenuating for both *P* and *S* waves compared to the rocks further away from it. The highly hydraulically conductive part of the NE-1 fracture system (NE-1-III) appears less attenuating compared with the low permeable and low water-bearing neighboring sets.

This study illustrates the potential of active-source surface-tunnel-surface seismic data to resolve structures between the tunnel and the surface. Additionally, it shows the potential of this approach to characterize fracture zones using various parameters such as *P* and *S* wave velocities, V_P/V_S, Poisson's ratio, and the quality factors Q_P and Q_S. At the Äspö site, the more hydraulically conductive fracture zone investigated by the seismic experiment is characterized by its higher velocities and higher *Q* value compared to the less conductive ones.

Acknowledgments

The seismic study presented here was carried out within the framework of the Trust2.2-GeoInfra (http://trust-geoinfra.se) project sponsored by Formas (project 252-2012-1907), BeFo, SBUF, Skanska, SGU, FQM, and NGI. B. Brodic thanks Formas, BeFo, SBUF, and Skanska for funding his PhD studies. We thank M. Bastani, J. Place, G. Maries, E. Lundberg, S. Wang, and M. Dehghannejad from the Geophysics Program of Uppsala University for their data acquisition contributions and helpful discussion before and during the fieldwork. SKB and Nova FoU partly sponsored this work for which we are grateful. We particularly thank M. Ask for initiating the project, Tyréns, and SKB personnel for providing support data and access to the underground facility. Lund University (and their partners) through the Trust 4.2 project provided the four sea source records used in this study for which we are thankful. GLOBE Claritas™ under license from the Institute of Geological and Nuclear Sciences Limited (GNS), Lower Hutt, New Zealand, was used to prepare and process the seismic data. GMT from P. Wessel and W.H.F. Smith and Seismic Un*x were used in this study. We thank A. Tryggvason for providing the *ps_tomo* tomography code. gOcad™ from Paradigm was used for 3-D visualization and viewing of the data and results. We thank the Associate Editor and two anonymous reviewers for their comments and suggestions that helped through a number of revisions to significantly improve the study presented in this paper. Regarding the data availability and sharing, contact Alireza Malehmir (alireza.malehmir@geo.uu.se).

References

Anderson, D. L., B. Minster, and D. Cole (1974), The effect of oriented cracks on seismic velocities, *J. Geophys. Res.*, *79*, 4011–4015, doi:10.1029/JB079i026p04011.

Andersson, C. J. (2007), *Äspö Hard Rock Laboratory, Äspö Pillar Stability Experiment, Final Report, Rock Mass Response to Coupled Mechanical Thermal Loading*, TR, 310 pp., Swedish Nuclear Waste Management Co. - SKB, Stockholm.

Angioni, T., R. D. Rechtien, S. J. Cardimona, and R. Luna (2003), Crosshole seismic tomography and borehole logging for engineering site characterization in Sikeston, MO, USA, *Tectonophysics*, *368*(1–4), 119–137, doi:10.1016/S0040-1951(03)00154-9.

Ask, D. (2006), Measurement-related uncertainties in overcoring data at the Äspö HRL, Sweden. Part 2: Biaxial tests of CSIRO HI overcore samples, *Int. J. Rock Mech. Min. Sci.*, *43*(1), 127–138, doi:10.1016/j.ijrmms.2005.05.012.

Ayarza, P., et al. (2000), Integrated geological and geophysical studies in the SG4 borehole area, Tagil volcanic arc, middle Urals: Location of seismic reflectors and source of the reflectivity, *J. Geophys. Res.*, *105*, 21,333–21,352, doi:10.1029/2000JB900137.

Badri, M., and H. Mooney (1987), *Q* measurements from compressional seismic waves in unconsolidated sediments, *Geophysics*, *52*(6), 772–784, doi:10.1190/1.1442344.

Barton, N. (2007), *Rock Quality, Seismic Velocity, Attenuation and Anisotropy*, 729 pp., Taylor & Francis Group, London, U. K.

Bellefleur, G., C. Müller, D. Snyder, and L. Matthews (2004), Downhole seismic imaging of a massive sulfide orebody with mode-converted waves, Halfmile Lake, New Brunswick, Canada, *Geophysics*, *69*(2), 318–329, doi:10.1190/1.1707051.

Bellefleur, G., A. Malehmir, and C. Müller (2012), Elastic finite-difference modeling of volcanic-hosted massive sulfide deposits: A case study from Half Mile Lake, New Brunswick, Canada, *Geophysics*, *77*(5), WC25–WC36, doi:10.1190/geo2011-0445.1.

Berglund, J., P. Curtis, T. Eliasson, T. Olsson, P. Starzec, and E.-L. Tullborg (2003), *Äspö Hard Rock Laboratory Update of the Geological Model 2002*, IPR, 130 pp., Swedish Nuclear Waste Management Co. - SKB, Stockholm.
Bergman, B., A. Tryggvason, and C. Juhlin (2004), High-resolution seismic traveltime tomography incorporating static corrections applied to a till-covered bedrock environment, *Geophysics*, *69*(4), 1082–1090.
Blake, O. O., and D. R. Faulkner (2016), The effect of fracture density and stress state on the static and dynamic bulk moduli of westerly granite, *J. Geophys. Res. Solid Earth*, *121*, 2382–2399, doi:10.1002/2015JB012310.
Boadu, F. K., and L. T. Long (1996), Effects of fractures on seismic-wave velocity and attenuation, *Geophys. J. Int.*, *127*(1), 86–110, doi:10.1111/j.1365-246X.1996.tb01537.x.
Bohlen, T., U. Lorang, W. Rabbel, C. Müller, R. Giese, S. Lüth, and S. Jetschny (2007), Rayleigh-to-shear wave conversion at the tunnel face—From 3D-FD modeling to ahead-of-drill exploration, *Geophysics*, *72*(6), T67–T79, doi:10.1190/1.2785978.
Brodic, B., A. Malehmir, C. Juhlin, L. Dynesius, M. Bastani, and H. Palm (2015), Multicomponent broadband digital-based seismic landstreamer for near-surface applications, *J. Appl. Geophys.*, *123*, 227–241, doi:10.1016/j.jappgeo.2015.10.009.
Carcione, J. M., and F. Cavallini (2002), Article details—Poisson's ratio at high pore pressure, *Geophys. Prospect.*, *50*(1), 97–106, doi:10.1046/j.1365-2478.2002.00299.x.
Crampin, S. (1981), A review of wave motion in anisotropic and cracked elastic-media, *Wave Motion*, *3*(4), 343–391.
Crampin, S. (1987), Geological and industrial implications of extensive-dilatancy anisotropy, *Nature*, *328*(6130), 491–496, doi:10.1038/328491a0.
Daley, T. M., E. L. Majer, and J. E. Peterson (2004), Crosswell seismic imaging in a contaminated basalt aquifer, *Geophysics*, *69*(1), 16–24, doi:10.1190/1.1649371.
Dasgupta, R., and R. Clark (1998), Estimation of *Q* from surface seismic reflection data, *Geophysics*, *63*(6), 2120–2128, doi:10.1190/1.1444505.
Dietrich, P., and J. Tronicke (2009), Integrated analysis and interpretation of cross-hole *P*- and *S*-wave tomograms: A case study, *Surf. Geophys.*, *7*(2), 101–109.
Dvorkin, J., G. Mavko, and A. Nur (1999), Overpressure detection from compressional- and shear-wave data, *Geophys. Res. Lett.*, *26*, 3417–3420, doi:10.1029/1999GL008382.
Eaton, D. W., B. Milkereit, and M. H. Salisbury (2003), *Hardrock Seismic Exploration*, *Geophys. Dev. Ser.*, No. 10, 270 pp., Soc. of Explor. Geophys., Tulsa, Okla.
Ekanem, A. M., J. Wei, X.-Y. Li, M. Chapman, and I. G. Main (2013), *P*-wave attenuation anisotropy in fractured media: A seismic physical modelling study, *Geophys. Prospect.*, *61*, 420–433, doi:10.1111/j.1365-2478.2012.01127.x.
Geldart, L. P., and R. E. Sheriff (2004), *Problems in Exploration Seismology and Their Solutions*, *Geophys. Ref. Ser.*, No. 14, 514 pp., Soc. of Explor. Geophys., Tulsa, Okla.
Green, A. G., and J. A. Mair (1983), Subhorizontal fractures in a granitic pluton; their detection and implications for radioactive waste disposal, *Geophysics*, *48*(11), 1428–1449, doi:10.1190/1.1441428.
Gritto, R., T. M. Daley, and E. L. Majer (2003), Estimating subsurface topography from surface-to-borehole seismic studies at the Rye Patch geothermal reservoir, Nevada, USA, *Geothermics*, *32*(3), 275–295, doi:10.1016/S0375-6505(03)00022-1.
Gritto, R., V. A. Korneev, T. M. Daley, M. A. Feighner, E. L. Majer, and J. E. Peterson (2004), Surface-to-tunnel seismic tomography studies at Yucca Mountain, Nevada, *J. Geophys. Res.*, *109*, B03310, doi:10.1029/2002JB002036.
Gustafson, G., R. Stanfors, and P. Wikberg (1989), *Swedish Hard Rock Laboratory Evaluation of 1988 Year Reinvestigations and Description of the Target Area, the Island of Äspö*, 152 pp., TR, Swedish Nuclear Waste Management Co. - SKB, Stockholm.
Hardage, B., M. DeAngelo, P. Murray, and D. Sava (2011), *Multicomponent Seismic Technology*, *Geophys. Ref. Ser.*, No. 18, 318 pp., Soc. of Explor. Geophys., Tulsa, Okla.
Harris, P. E., C. Kerner, and R. E. White (1997), Multichannel estimation of frequency-department *Q* from VSP data1, *Geophys. Prospect.*, *45*(1), 87–109, doi:10.1111/j.1365-2478.1997.tb02272.x.
Hole, J. A. (1992), Nonlinear high-resolution three-dimensional seismic travel time tomography, *J. Geophys. Res.*, *97*, 6553–6562, doi:10.1029/92JB00235.
Hole, J. A., and B. C. Zelt (1995), 3-D finite-difference reflection travel times, *Geophys. J. Int.*, *121*(2), 427–434, doi:10.1111/j.1365-246X.1995.tb05723.x.
Holliger, K., and J. Bühnemann (1996), Attenuation of broad-band (50–1500 Hz) seismic waves in granitic rocks near the Earth' surface, *Geophys. Res. Lett.*, *23*, 1981–1984, doi:10.1029/96GL01855.
Hudson, J. A. (1981), Wave speeds and attenuation of elastic waves in material containing cracks, *Geophys. J. Int.*, *64*(1), 133–150.
Johnston, D., M. Toksöz, and A. Timur (1979), Attenuation of seismic waves in dry and saturated rocks: II. Mechanisms, *Geophysics*, *44*(4), 691–711, doi:10.1190/1.1440970.
Juhlin, C. (1990), Seismic attenuation, shear wave anisotropy and some aspect of fracturing in the crystalline rock of the Siljan Ring area, central Sweden, Uppsala dissertations from the Faculty of Science ISSN 0346–6485, Doctoral thesis., Acta Universitatis Upsaliensis, Uppsala.
Juhlin, C. (1995a), Finite-difference elastic wave propagation in 2D heterogeneous transversely isotropic media, *Geophys. Prospect.*, *43*(6), 843–858, doi:10.1111/j.1365-2478.1995.tb00284.x.
Juhlin, C. (1995b), Imaging of fracture zones in the Finnsjon area, central Sweden, using the seismic reflection method, *Geophysics*, *60*(1), 66–75, doi:10.1190/1.1443764.
Juhlin, C., E. Sturkell, J. O. R. Ebbestad, O. Lehnert, A. E. S. Högström, and G. Meinhold (2012), A new interpretation of the sedimentary cover in the western Siljan Ring area, central Sweden, based on seismic data, *Tectonophysics*, *580*, 88–99, doi:10.1016/j.tecto.2012.08.040.
Kjartansson, E. (1979), Constant *Q*-wave propagation and attenuation, *J. Geophys. Res.*, *84*, 4737–4748, doi:10.1029/JB084iB09p04737.
Knopoff, L. (1964), Q, *Rev. Geophys.*, *2*, 625–660, doi:10.1029/RG002i004p00625.
Kong, L., B. Gurevich, T. M. Muller, Y. Wang, and H. Yang (2013), Effect of fracture fill on seismic attenuation and dispersion in fractured porous rocks, *Geophys. J. Int.*, *195*(3), 1679–1688, doi:10.1093/gji/ggt354.
Kornfält, K.-A., and H. Wikman (1988), *The Rocks of the Äspö Island. Description to the Detailed Maps of Solid Rocks Including Maps of Uncovered Trenches*, 280 pp., PR, Swedish Nuclear Waste Management Co. - SKB, Stockholm.
Kornfält, K.-A., P.-O. Persson, and H. Wikman (1997) *Granitoids from the Äspö Area, Southeastern Sweden—Geochemical and Geochronological Data*, 330 pp., GFF, Swedish Nuclear Waste Management Co. - SKB, Stockholm.
Liu, E., and A. Martinez (2013), *Seismic Fracture Characterization: Concepts and Practical Applications*, 279 pp., EAGE Education Tour EET 8, EAGE Publications bv, Houten, Nederlands.
Lundberg, E. (2014), *2D and 3D Reflection Seismic Studies over Scandinavian Deformation Zones*, 57 pp., Acta Universitatis Upsaliensis, Uppsala.
Lundberg, E., and C. Juhlin (2011), High resolution reflection seismic imaging of the Ullared deformation zone, southern Sweden, *Precambrian Res.*, *190*(1–4), 25–34, doi:10.1016/j.precamres.2011.07.012.

Lundberg, E., C. Juhlin, and A. Nasuti (2012), High resolution reflection seismic profiling over the Tjellefonna fault in the Møre-Trøndelag fault complex, Norway, *Solid Earth*, *3*(1), 175–188, doi:10.5194/se-3-175-2012.

Lüth, S., R. Giese, P. Otto, K. Krüger, S. Mielitz, T. Bohlen, and T. Dickmann (2008), Seismic investigations of the Piora Basin using *S*-wave conversions at the tunnel face of the Piora adit (Gotthard Base Tunnel), *Int. J. Rock Mech. Min. Sci.*, *45*(1), 86–93, doi:10.1016/j.ijrmms.2007.03.003.

Mair, J. A., and A. G. Green (1981), High-resolution seismic reflection profiles reveal fracture zones within a "homogeneous" granite batholith, *Nature*, *294*(5840), 439–442, doi:10.1038/294439a0.

Malehmir, A., and G. Bellefleur (2010), Reflection seismic imaging and physical properties of base-metal and associated iron deposits in the Bathurst mining camp, New Brunswick, Canada, *Ore Geol. Rev.*, *38*(4), 319–333, doi:10.1016/j.oregeorev.2010.08.002.

Malehmir, A., S. Wang, J. Lamminen, B. Brodic, M. Bastani, K. Vaittinen, C. Juhlin, and J. Place (2015a), Delineating structures controlling sandstone-hosted base-metal deposits using high-resolution multicomponent seismic and radio-magnetotelluric methods: A case study from northern Sweden, *Geophys. Prospect.*, *63*(4), 774–797, doi:10.1111/1365-2478.12238.

Malehmir, A., F. Zhang, M. Dehghannejad, E. Lundberg, C. Döse, O. Friberg, B. Brodic, J. Place, M. Svensson, and H. Möller (2015b), Planning of urban underground infrastructure using a broadband seismic landstreamer—Tomography results and uncertainty quantifications from a case study in southwestern Sweden, *Geophysics*, *80*(6), B177–B192, doi:10.1190/geo2015-0052.1.

Malehmir, A., S. Heinonen, M. Dehghannejad, P. Heino, G. Maries, F. Karell, M. Suikkanen, and A. Salo (2017), Landstreamer seismics and physical property measurements in the Siilinjärvi open-pit apatite (phosphate) mine, central Finland, *Geophysics*, *82*(2), B29–B48, doi:10.1190/geo2016-0443.1.

Martínez, K., and J. A. Mendoza (2011), Urban seismic site investigations for a new metro in central Copenhagen: Near surface imaging using reflection, refraction and VSP methods, *Phys. Chem. Earth Parts ABC*, *36*(16), 1228–1236, doi:10.1016/j.pce.2011.01.003.

Maurer, H., and A. G. Green (1997), Potential coordinate mislocations in crosshole tomography: Results from the Grimsel test site, Switzerland, *Geophysics*, *62*(6), 1696–1709, doi:10.1190/1.1444269.

Mavko, G., and A. Nur (1979), Wave attenuation in partially saturated rocks, *Geophysics*, *44*(2), 161–178, doi:10.1190/1.1440958.

Mavko, G., T. Mukerji, and J. Dvorkin (2009), *The Rock Physics Handbook: Tools for Seismic Analysis of Porous Media*, 511 pp., Cambridge Univ. Press, New York.

Melanson, D. M., D. J. White, C. Samson, G. Bellefleur, E. Schetselaar, and D. R. Schmitt (2015), Mode-converted volcanogenic massive sulphide ore lens reflections in vertical seismic profiles from Flin Flon, Manitoba, Canada: Mode-converted VMS ore lens reflections, *Geophys. Prospect.*, *63*(4), 849–860, doi:10.1111/1365-2478.12267.

Meléndez-Martínez, J., and D. R. Schmitt (2016), A comparative study of the anisotropic dynamic and static elastic moduli of unconventional reservoir shales: Implication for geomechanical investigations, *Geophysics*, *81*(3), D245–D261, doi:10.1190/geo2015-0427.1.

Mukerji, T., and G. Mavko (1994), Pore fluid effects on seismic velocity in anisotropic rocks, *Geophysics*, *59*(2), 233–244, doi:10.1190/1.1443585.

O'Connell, R. J., and B. Budiansky (1974), Seismic velocities in dry and saturated cracked solids, *J. Geophys. Res.*, *79*, 5412–5426, doi:10.1029/JB079i035p05412.

Paulsson, B., N. Cook, and T. McEvilly (1985), Elastic-wave velocities and attenuation in an underground granitic repository for nuclear waste, *Geophysics*, *50*(4), 551–570, doi:10.1190/1.1441932.

Place, J., A. Malehmir, K. Högdahl, C. Juhlin, and K. P. Nilsson (2015), Seismic characterization of the Grängesberg iron deposit and its mining-induced structures, central Sweden, *Interpretation*, *3*(3), SY41–SY56, doi:10.1190/INT-2014-0212.1.

Podvin, P., and I. Lecomte (1991), Finite difference computation of traveltimes in very contrasted velocity models: A massively parallel approach and its associated tools, *Geophys. J. Int.*, *105*(1), 271–284, doi:10.1111/j.1365-246X.1991.tb03461.x.

Pyrak-Nolte, L. J., L. R. Myer, and N. G. W. Cook (1990), Transmission of seismic waves across single natural fractures, *J. Geophys. Res.*, *95*, 8617–8638, doi:10.1029/JB095iB06p08617.

Rhén, I., G. Gustafson, R. Stanfors, and P. Wikberg (1997), *Äspö HRL–Geoscientific Evaluation 1997/5. Models Based on Site Characterization 1986–1995*, 428 pp., TR, Swedish Nuclear Waste Management Co. - SKB, Stockholm.

Ronczka, M., K. Hellman, T. Günther, R. Wisen, and T. Dahlin (2016), Electric resistivity and seismic refraction tomography, a challenging joint underwater survey at Äspö Hard Rock Laboratory, *Solid Earth Discuss.*, *1–22*, doi:10.5194/se-2016-157.

Rubino, J. G., and K. Holliger (2012), Seismic attenuation and velocity dispersion in heterogeneous partially saturated porous rocks: Mesoscopic effects and partial saturation, *Geophys. J. Int.*, *188*(3), 1088–1102, doi:10.1111/j.1365-246X.2011.05291.x.

Rydström, H., and L. Gereben (1989), *Seismic Refraction Survey on Äspö and Hålö*, 243 pp., PR, Swedish Nuclear Waste Management Co. - SKB, Stockholm.

Rønning, J. H. S., O. Kihle, J. O. Mogaard, and P. Walker (2003), *Simpevarp Site Investigation. Helicopter Borne Geophysics at Simpevarp, Oskarshamn, Sweden*, 287 pp., P, Swedish Nuclear Waste Management Co. - SKB, Stockholm.

Sheriff, R. (2002), *Encyclopedic Dictionary of Exploration Geophysics*, *Geophys. Ref. Ser.*, No. 1, 384 pp. Soc. of Explor. Geophys., Tulsa, Okla.

Siggins, A. F., and D. N. Dewhurst (2003), Saturation, pore pressure and effective stress from sandstone acoustic properties: Pore pressure and saturation in sandstones, *Geophys. Res. Lett.*, *30*(2), 1089, doi:10.1029/2002GL016143.

Sopher, D., C. Juhlin, F. Huang, M. Ivandic, and S. Lüth (2014), Quantitative assessment of seismic source performance: Feasibility of small and affordable seismic sources for long term monitoring at the Ketzin CO_2 storage site, Germany, *J. Appl. Geophys.*, *107*, 171–186, doi:10.1016/j.jappgeo.2014.05.016.

Stanfors, R., I. Rhén, E.-L. Tullborg, and P. Wikberg (1999), Overview of geological and hydrogeological conditions of the Äspö Hard Rock Laboratory site, *Appl. Geochem.*, *14*(7), 819–834.

Stephens, M. B. (2009), Synthesis of the bedrock geology in the Bergslagen region, Fennoscandian shield, south-central Sweden, Sveriges Geologiska Undersökning (SGU).

Stockwell, J. (1997), Free software in education: A case study of CWP/SU: Seismic Un*x, *Lead. Edge*, *16*(7), 1045–1050, doi:10.1190/1.1437723.

Thomsen, L. (1986), Weak elastic anisotropy, *Geophysics*, *51*(10), 1954–1966, doi:10.1190/1.1442051.

Thomsen, L. (2002), *Understanding Seismic Anisotropy in Exploration and Exploitation*, *Distinguished Instruct. Ser.*, No. 5, 252 pp., Soc. of Explor. Geophys. and Eur. Assoc. of Geosci. and Eng., Tulsa, Okla.

Toksöz, M., D. Johnston, and A. Timur (1979), Attenuation of seismic waves in dry and saturated rocks: I. Laboratory measurements, *Geophysics*, *44*(4), 681–690, doi:10.1190/1.1440969.

Tonn, R. (1991), The determination of the seismic quality factor Q from VSP data: A comparison of different computational methods, *Geophys. Prospect.*, *39*(1), 1–27.

Toverud, T., and B. Ursin (2005), Comparison of seismic attenuation models using zero-offset vertical seismic profiling (VSP) data, *Geophysics*, *70*(2), F17–F25, doi:10.1190/1.1884827.

Tryggvason, A., and N. Linde (2006), Local earthquake (LE) tomography with joint inversion for *P*- and *S*-wave velocities using structural constraints, *Geophys. Res. Lett.*, *33*, L07303, doi:10.1029/2005GL025485.

Tryggvason, A., S. T. Rögnvaldsson, and Ó. G. Flóvenz (2002), Three-dimensional imaging of the *P*- and *S*-wave velocity structure and earthquake locations beneath Southwest Iceland, *Geophys. J. Int.*, *151*(3), 848–866, doi:10.1046/j.1365-246X.2002.01812.x.

Wahlgren, C.-H., J. Hermanson, O. Forssberg, P. Curtis, H. Drake, and E.-L. Tullborg (2006), *Geological Description of Rock Domains and Deformation Zones in the Simpevarp and Laxemar Subareas*, 271 pp., R, Swedish Nuclear Waste Management Co. - SKB, Stockholm.

Wang, Y. (2008), *Seismic Inverse Q Filtering*, 248 pp., Blackwell, Malden, Mass.

Wang, X.-Q., A. Schubnel, J. Fortin, E. C. David, Y. Guéguen, and H.-K. Ge (2012), High Vp/Vs ratio: Saturated cracks or anisotropy effects?, *Geophys. Res. Lett.*, *39*, L11307, doi:10.1029/2012GL051742.

Worthington, M. H., and J. A. Hudson (2000), Fault properties from seismic *Q*, *Geophys. J. Int.*, *143*(3), 937–944, doi:10.1046/j.1365-246X.2000.00315.x.

Xu, C., and R. Stewart (2006), Seismic attenuation (*Q*) estimation from VSP data, CSEG National Convention, Extended Abstracts, pp. 268–277, Citeseer.

Yardley, G. S., and S. Crampin (1991), Extensive-dilatancy anisotropy: Relative information in VSPs and reflection surveys1, *Geophys. Prospect.*, *39*(3), 337–355.

Yordkayhun, S., A. Tryggvason, B. Norden, C. Juhlin, and B. Bergman (2009), 3D seismic traveltime tomography imaging of the shallow subsurface at the CO_2 SINK project site, Ketzin, Germany, *Geophysics*, *74*(1), G1–G15, doi:10.1190/1.3026553.